RIOJA. Complex Dusty Starbursts in a Major Merger B14-65666 at <i>z</i>=7.15

Citation for the original published paper (version of record):
Sugahara, Y., Álvarez-Márquez, J., Hashimoto, T. et al (2025). RIOJA. Complex Dusty Starbursts in a Major Merger B14-65666 at <i>z</i>=7.15. Astrophysical Journal, 981(2).
http://dx.doi.org/10.3847/1538-4357/adb02a

The Astrophysical Journal, 981:135 (18pp), 2025 March 10 https://doi.org/10.3847/1538-4357/adb02a

RIOJA. Complex Dusty Starbursts in a Major Merger B14-65666 at $z = 7.15$

Yuma Sugahara[1,2,3], Javier Álvarez-Márquez[4], Takuya Hashimoto[5,6], Luis Colina[4], Akio K. Inoue[2,3], Luca Costantin[4], Yoshinobu Fudamoto[1,2,7], Ken Mawatari[5,6], Yi W. Ren[3], Santiago Arribas[4], Tom J. L. C. Bakx[8], Carmen Blanco-Prieto[4], Daniel Ceverino[9,10], Alejandro Crespo Gómez[4], Masato Hagimoto[11], Takeshi Hashigaya[12], Rui Marques-Chaves[13], Hiroshi Matsuo[1,14], Yurina Nakazato[15], Miguel Pereira-Santaella[16], Yoichi Tamura[11], Mitsutaka Usui[5], and Naoki Yoshida[15,17,18]

[1] National Astronomical Observatory of Japan, 2-21-1 Osawa, Mitaka, Tokyo 181-8588, Japan; sugayu@aoni.waseda.jp
[2] Waseda Research Institute for Science and Engineering, Faculty of Science and Engineering, Waseda University, 3-4-1 Okubo, Shinjuku, Tokyo 169-8555, Japan
[3] Department of Pure and Applied Physics, School of Advanced Science and Engineering, Faculty of Science and Engineering, Waseda University, 3-4-1 Okubo, Shinjuku, Tokyo 169-8555, Japan
[4] Centro de Astrobiología (CAB), CSIC-INTA, Ctra. de Ajalvir km 4, Torrejón de Ardoz, E-28850, Madrid, Spain
[5] Division of Physics, Faculty of Pure and Applied Sciences, University of Tsukuba, Tsukuba, Ibaraki 305-8571, Japan
[6] Tomonaga Center for the History of the Universe (TCHoU), Faculty of Pure and Applied Sciences, University of Tsukuba, Tsukuba, Ibaraki 305-8571, Japan
[7] Center for Frontier Science, Chiba University, 1-33 Yayoi-cho, Inage-ku, Chiba 263-8522, Japan
[8] Department of Space, Earth and Environment, Chalmers University of Technology, Onsala Space Observatory, SE-439 92 Onsala, Sweden
[9] Universidad Autonoma de Madrid, Ciudad Universitaria de Cantoblanco, E-28049 Madrid, Spain
[10] CIAFF, Facultad de Ciencias, Universidad Autonoma de Madrid, E-28049 Madrid, Spain
[11] Department of Physics, Graduate School of Science, Nagoya University, Nagoya, Aichi 464-8602, Japan
[12] Department of Astronomy, Kyoto University Sakyo-ku, Kyoto 606-8502, Japan
[13] Geneva Observatory, Department of Astronomy, University of Geneva, Chemin Pegasi 51, CH-1290 Versoix, Switzerland
[14] The Graduate University for Advanced Studies (SOKENDAI), 2-21-1 Osawa, Mitaka, Tokyo 181-8588, Japan
[15] Department of Physics, The University of Tokyo, 7-3-1 Hongo, Bunkyo, Tokyo 113-0033, Japan
[16] Instituto de Física Fundamental (IFF), CSIC, Serrano 123, E-28006, Madrid, Spain
[17] Kavli Institute for the Physics and Mathematics of the Universe (WPI), UT Institute for Advanced Study, The University of Tokyo, Kashiwa, Chiba 277-8583, Japan
[18] Research Center for the Early Universe, School of Science, The University of Tokyo, 7-3-1 Hongo, Bunkyo, Tokyo 113-0033, Japan

Received 2024 March 25; revised 2024 December 2; accepted 2025 January 29; published 2025 March 4

Abstract

We present JWST NIRCam imaging of B14-65666 (“Big Three Dragons”), a bright Lyman-break galaxy system ($M_{\rm UV} = -22.5$ mag) at $z = 7.15$. The high angular resolution of NIRCam reveals the complex morphology of two galaxy components: galaxy E has a compact core (E-core), surrounded by diffuse, extended, rest-frame optical emission, which is likely to be tidal tails; and galaxy W has a clumpy and elongated morphology with a blue UV slope ($\beta_{\rm UV} = -2.2 \pm 0.1$). The flux excess, F356W − F444W, peaks at the E-core ($1.05^{+0.08}_{-0.09}$ mag), tracing the presence of strong [O III] $\lambda\lambda$4960,5008 emission. Atacama Large Millimeter/submillimeter Array archival data show that the bluer galaxy W is brighter in dust continua than the redder galaxy E, while the tails are bright in [O III] 88 μm. The UV/optical and submillimeter spectral energy distribution (SED) fitting confirms that B14-65666 is a major merger in a starburst phase as derived from the stellar mass ratio (3:1 to 2:1) and the star formation rate, $\simeq$1 dex higher than the star formation main sequence at the same redshift. Galaxy E is a dusty ($A_{\rm V} = 1.2 \pm 0.1$ mag) starburst with a possible high dust temperature ($\geqslant$63–68 K). Galaxy W would have a low dust temperature ($\leqslant$27–33 K) or patchy stellar-and-dust geometry, as suggested by the IR excess and $\beta_{\rm UV}$ diagram. The high optical-to-far-IR [O III] line ratio of the E-core shows its lower gas-phase metallicity ($\simeq$0.2–0.4 $Z_\odot$) than galaxy W. These results agree with a scenario where major mergers disturb morphology and induce nuclear dusty starbursts triggered by less-enriched inflows. B14-65666 shows a picture of complex stellar buildup processes during major mergers in the epoch of reionization.

Unified Astronomy Thesaurus concepts: Galaxy evolution (594); High-redshift galaxies (734); Galaxy mergers (608); Near infrared astronomy (1093)

1. Introduction

Galaxy mergers are a fundamental process to build up the stellar content through galaxy evolution. Gravitational perturbations by galaxy interactions can strongly disturb the morpho-kinematics, which is characterized by tidal tails and large velocity dispersion. It is theoretically predicted that such perturbation promotes gas accretion from the outskirts into the central parts of galaxies that can trigger nuclear star formation (J. C. Mihos & L. Hernquist 1994, 1996; J. E. Barnes & L. Hernquist 1996). In observations of local galaxies, the star formation rate (SFR) of interacting galaxies increases as projected pair separation decreases to within several tens kiloparsecs (e.g., E. J. Barton et al. 2000). This SFR enhancement is particularly notable in collisions of galaxies with similar stellar masses (i.e., “major mergers”; e.g., S. L. Ellison et al. 2008). The gas accretion associated with mergers can also induce an observed reduction in the gas-phase metallicity at a fixed mass or luminosity (e.g., L. J. Kewley et al. 2006; S. L. Ellison et al. 2008). Even after the coalescence phase, the major mergers are expected to cause energetic events in the subsequent evolution of the merged galaxies, such as luminous IR starbursts, rapid black hole growths, and the appearance of quasars (P. F. Hopkins et al. 2008).

At high redshifts, major mergers are predicted to play a more important role in the evolutionary path because the merger rate theoretically increases with increasing redshift by $\propto (1 + z)^{2-3}$ (e.g., O. Fakhouri & C.-P. Ma 2008; V. Rodriguez-Gomez et al. 2015). This increase is consistent with observed major merger fractions at $z \sim 0$–5 (e.g., A. W. S. Man et al. 2016; E. Ventou et al. 2017) when the redshift-dependent merger timescale is taken into account (Y. Qu et al. 2017; G. F. Snyder et al. 2017; M. Romano et al. 2021). Recently, rest-frame UV images (B. Ribeiro et al. 2017; K. Duncan et al. 2019; T. Shibuya et al. 2022) and [C II] 158 μm data cubes (M. Romano et al. 2021) were able to explore the merger fractions up to $z \sim 5$–7. Although the measured fractions are yet to be converged and depend strongly on galaxy masses, the high merger fraction, 20%–80% at $z \sim 5$–7, supports a large number of galaxies that experienced major mergers in the early Universe. In terms of the stellar mass assembly, contributions of major mergers are suggested to be comparable to in situ star formation at $z > 3$ (K. Duncan et al. 2019; M. Romano et al. 2021; Q. Duan et al. 2024). While cosmological zoom-in simulations also support the SFR enhancement by gas-rich mergers at $z > 5$ (D. Ceverino et al. 2018), the effect of mergers on star formation appears to reduce strongly from the local Universe to $z \sim 1$–3 (e.g., A. Silva et al. 2018; E. A. Shah et al. 2022).

High angular resolution is key to pushing up the redshift frontier of merger studies. Merging systems at $z \gtrsim 5$ are reported from observations of the Hubble Space Telescope (HST), the James Webb Space Telescope (JWST; J. P. Gardner et al. 2023), and the Atacama Large Millimeter/submillimeter Array (ALMA), which have both high angular resolutions and highest sensitivities that can resolve high-redshift galaxies. For example, dusty systems at $z \sim 4$–7 corresponding to hyper/ultraluminous IR galaxies (ULIRGs) sometimes show signatures of galaxy mergers (e.g., I. Oteo et al. 2016; D. P. Marrone et al. 2018; A. P. S. Hygate et al. 2023; A. Bik et al. 2024). Triple mergers have also been observed, such as a dust-free, luminous Lyα emitter at $z = 6.6$ (“Himiko,” M. Ouchi et al. 2013) and the [C II]-bright galaxy at $z = 4.6$ (G. C. Jones et al. 2020a). JWST has recently updated the most distant major merger by spectroscopically confirming a triply lensed galaxy at $z = 10.17$ that has clumps with different dust attenuation (T. Y.-Y. Hsiao et al. 2023, 2024). For a statistical study, JWST has shown that galaxy interactions significantly contribute to the bursty star formation and strong emission lines in low-mass galaxies at $z \sim 5$–6 (Y. Asada et al. 2024). However, few merging galaxies are observed and detected with multiple bands in both UV and far-IR (FIR), limiting our ability to interpret the complete properties of distant merging systems.

Multiwavelength, high-angular-resolution observations are essential to examine the complex properties of stars, gas, and dust through UV-to-FIR spectral energy distributions (SEDs) of resolved galaxy components. Red colors of high-redshift galaxies are generally tied with dust attenuation similar to local star-forming galaxies (R. A. A. Bowler et al. 2022), but some galaxies exhibit spatially patchy geometry of UV, line, and dust emission (e.g., L. Colina et al. 2023; Y. Tamura et al. 2023). This complexity as well as undetermined dust attenuation curves at high redshift strengthens the importance of multiwavelength observations. Under these circumstances, combinations of JWST and ALMA observations offer valuable constraints on SEDs of spatially resolved galaxies. JWST near-IR observations uncover resolved stellar and gaseous properties of galaxies even at $z > 6$ (Abdurro’uf et al. 2023; C. Giménez-Arteaga et al. 2023). Dust detections with (multiple) ALMA bands help break the degeneracy between the star formation age and dust attenuation by constraining the dust temperature and FIR SFR (e.g., T. J. L. C. Bakx et al. 2021; J. Álvarez-Márquez et al. 2023; A. Crespo Gómez et al. 2024; J. Li et al. 2024). Moreover, these combinations allow us to estimate the nebular properties of the interstellar media with optical-to-FIR emission-line ratios (M. Stiavelli et al. 2023; S. Fujimoto et al. 2024). Thus, the synergy between JWST and ALMA effectively works in revealing the complex properties of merging galaxies during the epoch of reionization (EoR).

This paper presents new observations of a bright merging galaxy system at $z = 7.15$, B14-65666, also known as the Big Three Dragons (T. Hashimoto et al. 2019), with NIRCam (M. J. Rieke et al. 2023) on board JWST. These observations were conducted as part of the RIOJA project: “the Reionization and the ISM/Stellar Origins with JWST and ALMA” (JWST GO1 PID1840; PIs: J. Álvarez-Márquez and T. Hashimoto; J. Álvarez-Márquez et al. 2021; T. Hashimoto et al. 2023a). Combining ALMA ancillary data with the NIRCam images, we investigate stellar, gaseous, and dusty properties in morphology and star formation of B14-65666. This paper is organized as follows. Section 2.2 describes NIRCam, ancillary data, and the reduction processes. Section 3 explains analysis tools including image analyses, SED fitting, and photoionization models. Section 4 presents results about morphology, comparison with ALMA data, and SED fitting. Section 5 discusses relations between UV and FIR photometry, a metallicity distribution, and our interpretations of B14-65666. Finally, Section 6 summarizes our conclusions. Throughout this paper, we use the AB magnitude system (J. B. Oke & J. E. Gunn 1983) and the flat ΛCDM cosmology ($\Omega_{\rm M} = 0.310$ and $h = H_0/[100\,{\rm km\,s^{-1}\,Mpc^{-1}}] = 0.677$; Planck Collaboration et al. 2020). At $z = 7.15$, $1''$ corresponds to 5.27 kpc.

2. Observations

2.1. Summary of Previous Observations of B14-65666

B14-65666 was first identified as a Lyman-break galaxy from the UltraVISTA survey (R. A. A. Bowler et al. 2012, 2014). Its UV absolute magnitude of $M_{\rm UV} = -22.5$ mag is 4 times brighter than the characteristic value at $z = 7$ ($M^*_{\rm UV} \simeq -21.0$ mag; e.g., S. L. Finkelstein et al. 2015; R. J. Bouwens et al. 2021). Multiwavelength follow-up observations were conducted to detect the Lyα emission line (H. Furusawa et al. 2016), the UV continuum with high spatial resolution (R. A. A. Bowler et al. 2017), the [O III] 88 μm and [C II] 158 μm emission lines (T. Hashimoto et al. 2019), and dust continua at 88, 122, and 158 μm (R. A. A. Bowler et al. 2018; T. Hashimoto et al. 2019; Y. Sugahara et al. 2021). From the dust continua, the IR luminosity is estimated to be $\log L_{\rm IR}/L_\odot = 11.6^{+0.6}_{-0.3}$ at the dust emissivity of $\beta_{\rm d} = 2.0$ (Y. Sugahara et al. 2021). The galaxy was also observed by ALMA Bands 3 and 7, but it remained undetected in CO(6–5), CO(7–6), [C I](2–1) (T. Hashimoto et al. 2023b) and [N II] 122 μm (Y. Sugahara et al. 2021). The systemic redshift was determined from the [O III] and [C II] emission lines to be $z = 7.1520 \pm 0.0003$ (T. Hashimoto et al. 2019). These observations do not provide any evidence of the presence of an active galactic nucleus (AGN) in the B14-65666

Table 1
Summary of NIRCam and ALMA Observations

Band	$\lambda_{\rm rest}$	PSF FWHM (arcsec)	5σ Depth
NIRCam/F115W	1416 Å	0.060	23.3 nJy
NIRCam/F150W	1841 Å	0.067	7.7 nJy
NIRCam/F200W	2441 Å	0.076	23.5 nJy
NIRCam/F277W	3418 Å	0.13	20.4 nJy
NIRCam/F356W	4371 Å	0.15	19.5 nJy
NIRCam/F444W	5424 Å	0.16	15.4 nJy
ALMA/Band 8	88.84 μm	0.39×0.36	141 μJy beam^{-1}
ALMA/Band 7	122.6 μm	1.17×0.98	45.5 μJy beam^{-1}
ALMA/Band 6	158.7 μm	0.28×0.20	42.3 μJy beam^{-1}

Note. The rest-frame wavelengths, $\lambda_{\rm rest}$, are converted from the pivot wavelengths for NIRCam. The 5σ depths are computed within $2\times$PSF-FWHM diameter apertures for NIRCam and with a peak rms for ALMA.

system. We use our new NIRCam data and the ancillary data to investigate detailed merger properties during EoR.

2.2. JWST and ALMA Observations and Data Reductions

The NIRCam images of B14-65666 were taken on 2022 December 20 with a total exposure time of 644 s in F200W and F277W, 730 s in F115W and F356W, and 1675 s in F150W and F444W. The F115W, F200W, F277W, and F356W observations adopted the BRIGHT1 readout pattern with eight or nine groups and one integration; the F150W and F444W observations adopted the SHALLOW4 with eight groups in one integration. All the exposures were four times dithered using the INTRAMODULEBOX pattern. In the RIOJA project, the NIRCam filters were selected such as to trace the continuum emission over the entire 1–5 μm wavelength range with mostly avoiding the contamination by the main optical emission lines. Given the spectroscopic redshift of $z = 7.1520$, the short-wavelength channels of F115W, F150W, and F200W correspond to the rest-frame UV (1400–2500 Å). The F277W and F356W bands cover the stellar continua on both sides of the Balmer break without any contamination of strong optical emission lines. The F444W band includes the Hβ and [O III] $\lambda\lambda$4960,5008 emission lines as well as the underlying stellar continuum.

The data were reduced using our custom pipeline based on the JWST calibration pipeline version 1.9.4 (H. Bushouse et al. 2023) under CRDS context jwst_1041.pmap. Our additional reduction steps are: (1) snowballs and wisps removal as described in M. B. Bagley et al. (2023) and (2) background homogenization (including $1/f$-noise subtraction) applied in P. G. Pérez-González et al. (2023). The pixel scales of the final products for all the filters are set to $0''.03$/pixel. The measured angular resolution and 5σ depths of the NIRCam filters are listed in Table 1. We note that although the HST image has a comparable depth to the NIRCam ones, we did not use it in this study to avoid potential systematics among the telescope.

The ALMA data used in this work were presented in previous studies. ALMA Bands 6 and 8 data were taken in Cycles 4 (ID 2016.1.00954.S, PI: A. K. Inoue) and 5 (ID 2017.1.00190.S, PI: A. K. Inoue) to target the [C II] 158 μm and [O III] 88 μm emission lines (T. Hashimoto et al. 2019). ALMA Band 7 data were taken in Cycle 7 (ID: 2019.1.01491.S, PI: A. K. Inoue) to target the [N II] 122 μm emission line (Y. Sugahara et al. 2021). In all the observations, one of the four spectral windows was placed to observe the targeted lines while the others were for the underlying dust continua. The raw data were reduced with standard scripts on Common Astronomy Software Applications (CASA Team et al. 2022). [O III] and [C II] emission-line maps (i.e., moment-0 maps) were created by integrating wavelength ranges of $\simeq 600$ km s^{-1} around the line centers after the continuum subtraction (T. Hashimoto et al. 2019). Dust-continuum maps were created using channels that are unaffected by the emission lines. The synthesized beam FWHM is $0''.29 \times 0''.23$, $1''.15 \times 0''.97$, and $0''.39 \times 0''.37$ in Bands 6, 7, and 8 observations with the natural weighting. More information on the observations and data reduction is described in the references above. We did not use ALMA Band 3 data (ID: 2018.1.01673.S, PI: T. Hashimoto; T. Hashimoto et al. 2023b) in this study because neither continuum nor lines were detected and they do not give strong constraints on the FIR SED. The beam sizes and 5σ depths for the peak signal-to-noise ratio (S/N) of the ALMA observations are listed in Table 1.

Astrometry of the NIRCam images was corrected with stars in the field of view (FoV). In the NIRCam FoV, there exist three stars listed on the Gaia Data Release 3 main catalog (Gaia Collaboration et al. 2016, 2023). We aligned the NIRCam images to the three Gaia stars, and then we corrected small offsets between the NIRCam images using faint stars. The astrometric uncertainties of the NIRCam images are $<0''.015$. The peak positional accuracy of ALMA data, which can be estimated from the beam size and peak S/N,[19] is $\sim 0''.03$ for [C II] 158 μm and [O III] 88 μm line maps and $\sim 0''.06$ for dust continuum maps at 158 and 88 μm. As these estimates for the ALMA data are based on an equation for compact sources, the accuracy may be worse for extended sources like B14-65666.

3. Analyses

3.1. Image Analyses

When comparing different bands of the NIRCam images pixel by pixel, we matched the point spread functions (PSFs) of the images to that of the F444W image by kernel convolution. We constructed effective PSFs following the J. Anderson & I. R. King (2000) and J. Anderson (2016) methods using `photutils` (L. Bradley et al. 2023), which construct empirical models by fitting pixel values in images of stars detected with `IRAFStarFinder`. Then, we homogenized the PSFs of the NIRCam images using kernels created by `PyPHER` (A. Boucaud et al. 2016). We have checked that the PSF homogenization works well using faint stars in FoVs. Finally, the image pixels were resampled using `reproject` to match the F444W image pixels. When comparing the NIRCam and ALMA [O III] images, the PSFs of the NIRCam images are homogenized to the synthesized clean beam (i.e., two-dimensional Gaussian) of the ALMA images following the same procedure. The ALMA image pixels are resampled to match the F444W image pixels.

Photometry was performed with fixed apertures on the PSF-homogenized images and aperture correction was not applied. We chose a circular aperture of $1''.8$ in diameter to measure the total photometry of B14-65666, which sufficiently recovered all the fluxes according to curve-of-growth plots of

---

[19] Equation (10.7) in ALMA Cycle 10 Technical Handbook: https://almascience.nao.ac.jp/documents-and-tools/cycle10/alma-technical-handbook.

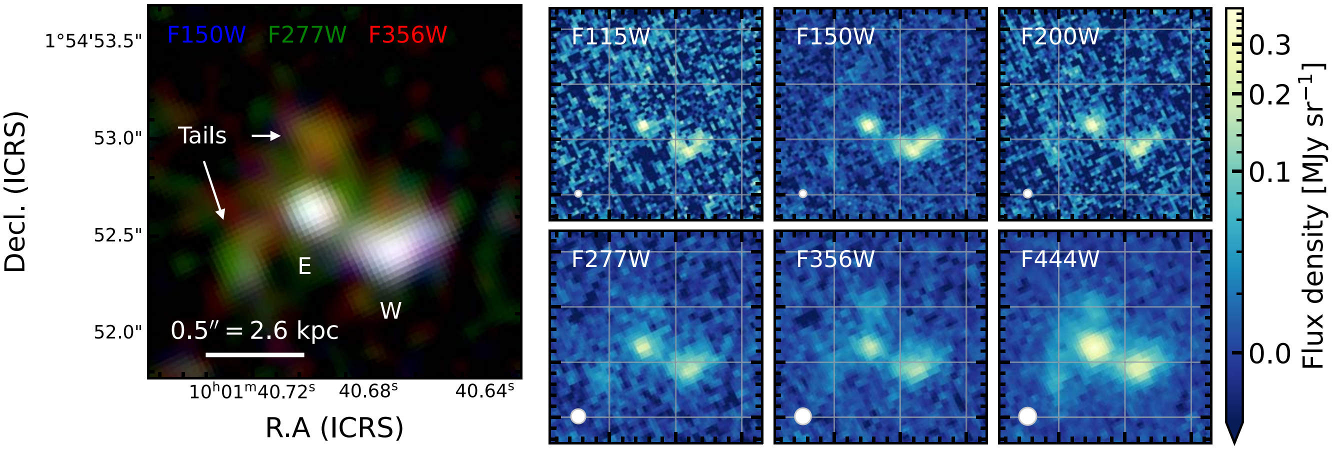

Figure 1. Left: pseudo-RGB composite image of B14-65666, where F356W (red), F277W (green), and F150W (blue) bands reflect continuum light. The RGB images are convolved to match the spatial resolution of the F444W-band image. B14-65666 shows complex morphology including the elongated galaxy W and galaxy E, which has a compact core that is surrounded by the red tails. Right: NIRCam-band stamps of B14-65666, which show the same sky area as the left panel; the grid intervals are 0.″6 in R.A. and 0.″5 in decl. They are illustrated in the native PSFs, which are shown with the white circles at the bottom left.

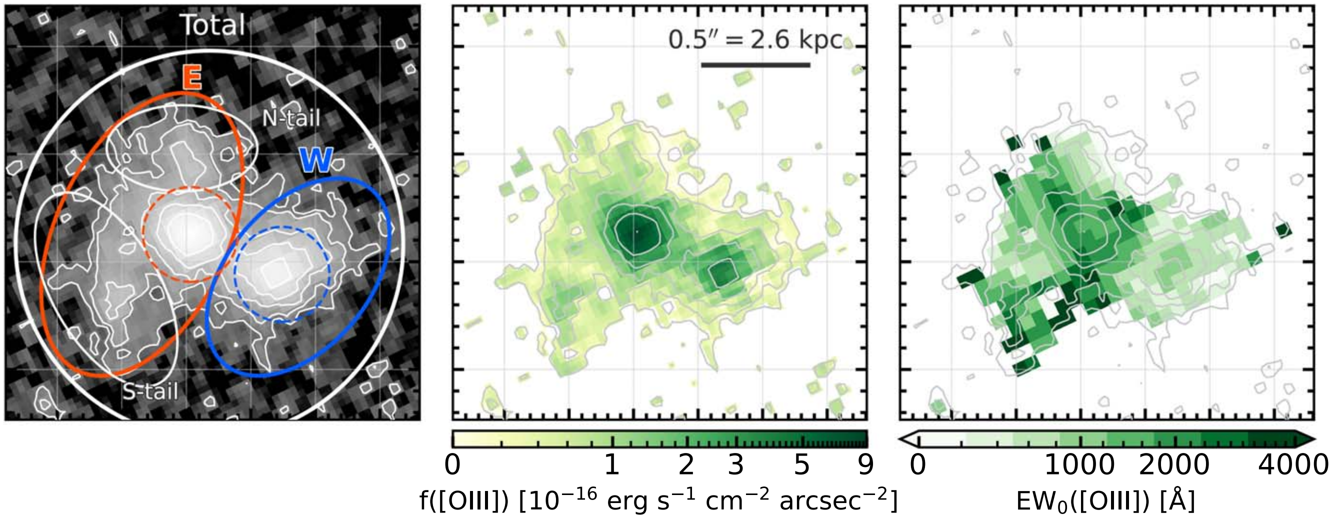

Figure 2. Left: apertures used for photometry of different components in B14-65666, on the F444W image. The total aperture (white) contains flux from the entire system, and galaxies E and W are represented with red and blue circles, respectively. The cores of the galaxies are depicted with the dashed circles. The thin white circles show the tails (N-tail and S-tail). The background contours are at the $2^n\sigma$ significance levels ($n = 1, 2, 3, \ldots$). Middle: [O III] $\lambda\lambda$4960,5008 flux map estimated from the F356W and F444W images (see text for details). The flux map is drawn in pixels with $S/N > 2$ in the F444W image. The gray contours are the F444W flux map, which is the same as in the left panel. Right: rest-frame [O III] equivalent width map, which is rebinned to improve S/N per pixel. The equivalent widths are estimated by dividing the flux map by the stellar continuum inferred from F356W. The [O III] fluxes reach the peaks at the cores of galaxies E and W. The rest-equivalent width values are $\mathrm{EW_0([O\,III])} = 2050 \pm 290$ and 740 ± 170 Å for the E-core and W-core, respectively, which implies the presence of the nuclear starbursts induced by the major merger. The equivalent widths in the tails are not significant in the 3σ level (Table 3).

the flux density. Because B14-65666 has a complex structure with several components and diffuse emission (see Section 4 and Figure 1), smaller apertures are used to measure the photometry of these individual components (see Figure 2). The local sky background computed in an annulus from 0.″95 to 1.″95 was subtracted before the photometry measurements. The photometric uncertainties were estimated from random aperture photometry. We scattered the apertures over the images around B14-65666 where bright objects are masked and we computed the uncertainties as the standard deviation of the aperture-photometry distributions. In addition, the absolute flux uncertainty was included in the photometric uncertainties as a conservative value of 5% (J. Rigby et al. 2023).[20]

3.2. SED Fitting

We performed SED fitting to the NIRCam photometry using Bayesian Analysis of Galaxies for Physical Inference and Parameter EStimation (`Bagpipes`; A. C. Carnall et al. 2018). We tested SED fitting with and without ALMA fluxes to see changes in obtained best-fit parameters. The ALMA [O III] 88 μm line and continuum fluxes were taken from T. Hashimoto et al. (2019). We note that these ALMA fluxes were measured by fitting two Gaussian components to the line and continuum maps, which differs from the aperture photometry for the NIRCam images. The redshift is fixed at $z = 7.1520$ in the fitting.

The fitting parameters are the star formation age t_{SF}, the stellar mass M_*, the ionization parameter U, the V-band dust attenuation A_{V}, the stellar metallicity Z_*, and the mass of an old stellar component M_{old}. The star formation history of B14-65666 is

---

[20] See also "NIRCam Imaging Calibration Status" in the JWST User Documentation for the current photometric calibration: https://jwst-docs.stsci.edu.

simply assumed to be constant for $t_{\rm SF}$ down to $z = 7.1520$. We also tested different star formation histories, but the fitting results were insensitive to different star formation histories (Appendix) because B14-65666 is dominated by a young bursty star formation of a $\sim$10 Myr timescale. The gas-phase metallicity is assumed to be identical to the stellar metallicity. The ionization parameter U controls nebular emission-line ratios, which is implemented using a photoionization code CLOUDY (G. J. Ferland et al. 1998, 2017). The hydrogen density in the CLOUDY models is fixed to be $n_{\rm H} = 100\,{\rm cm}^{-3}$ in `Bagpipes`. The dust attenuation curve follows the D. Calzetti et al. (2000) law. In addition, considering that B14-65666 is a major merger, stellar components older than recent starbursts should exist. To constrain the mass of the old stellar components, we added another constant star formation lasting for 500 Myr, from 600 to 100 Myr ago with respect to $z = 7.15$, which does not strongly contribute to UV continuum and emission-line fluxes. This selected star formation timescale is arbitrary, but changes in this timescale do not affect our conclusion. The stellar metallicity of the old components is fixed to $Z_{\rm star} = 0.5 Z_\odot$ (assuming that $Z = 0.02$ for solar metallicity; M. Asplund et al. 2021) to reduce the number of free parameters, but we checked that results do not vary significantly with the assumed $Z_{\rm star}$ value. The best-fit parameters are computed as the median of the posterior distributions. The 1σ fitting uncertainties are evaluated from the 16 and 84 percentiles of the posterior distributions.

For FIR SED, we added fitting parameters of the minimum stellar intensity $\mathcal{U}_{\rm min}$ and the fraction γ of the dust mass heated by $\mathcal{U} > \mathcal{U}_{\rm min}$. `Bagpipes` has adopted the B. T. Draine & A. Li (2007) dust emission models. Instead of the originally adopted ones, we used the updated version (B. T. Draine et al. 2014) implemented in the `CIGALE` SED fitting code (M. Boquien et al. 2019), which allows up to $\mathcal{U}_{\rm min} = 50$. The model parameters other than $\mathcal{U}_{\rm min}$ and γ were fixed: the power-law index of the stellar intensity $\alpha_{\mathcal{U}} = 2$, the maximum stellar intensity $\mathcal{U}_{\rm max} = 10^7$, and the polycyclic aromatic hydrocarbon (PAH) mass fraction $q_{\rm PAH} = 2.5\%$. The former two fixed parameters are appropriate to reproduce high-redshift galaxies (D. Burgarella et al. 2022) as well as nearby galaxies (B. T. Draine et al. 2014) and the latter $q_{\rm PAH}$ was fixed because our observations are insensitive to mid-IR wavelengths. We note that while we added two fitting parameters for the FIR SED, dust continua are constrained at only 2–3 bands. Thus, adding ALMA dust continua in the SED fitting is not quite effective in constraining the stellar properties better (as shown in Section 4.3), but it helps estimate the dust temperature necessary for the energy balance between dust attenuation and emission.

For input stellar models, the Binary Population and Spectral Synthesis code (`BPASS`; J. J. Eldridge et al. 2017) version 2.3 (C. M. Byrne et al. 2022) was used. `BPASS` includes effects of binary populations, which are important to reproduce strong [O III] emission lines observed at high redshift (Y. Sugahara et al. 2022). In particular, version 2.3 implements high α/Fe cases, reflecting abundance patterns found at $z \gtrsim 2$ dominated by core-collapse supernovae (C. C. Steidel et al. 2014, 2016). This enhancement of α elements is also key to reproducing [O III] emission-line strengths and hard UV spectral slopes at high redshift (e.g., A. E. Shapley et al. 2019; Y. Sugahara et al. 2022). We used the case of $\Delta \log(\alpha/{\rm Fe}) = +0.6$, where the oxygen abundance is almost the solar value $12 + \log {\rm O/H} = 8.69$ (M. Asplund et al. 2021) at $Z = 0.02$ (C. M. Byrne et al. 2022). The adopted initial mass function (IMF) is a P. Kroupa (2001) IMF in the mass range from 0.1 to 300 $M_\odot$. Their choice of the upper mass limit leads to a 45% higher ionizing flux and stronger hydrogen recombination lines than a choice of an upper limit of 100 $M_\odot$ (E. R. Stanway et al. 2016). The nebular-continuum and emission-line models are generated based on these stellar models.

3.3. Photoionization Models with CLOUDY

In our emission-line modeling, we used a photoionization code CLOUDY version 17.02 (G. J. Ferland et al. 1998, 2017). We note that our setup is more flexible than the one used in the `Bagpipes` SED fitting, by including an additional free parameter of $n_{\rm H}$. We assumed a plane-parallel geometry under the constant pressure and elemental and dust-grain abundances in the H II regions that are stored in CLOUDY. For the helium abundance, we simply added stellar yields to Big Bang nucleosynthesis as a function of the gas-phase metallicity (B. A. Groves et al. 2004). The input ionizing spectra were constructed from the `BPASS` version 2.3 and the stellar metallicity is assumed to be identical to the gas-phase metallicity. The star formation history is set to be a 10 Myr constant star formation. Adopted variable parameters are the ionization parameter U and hydrogen density $n_{\rm H}$ at the illuminated surface, and the gas-phase metallicity $Z_{\rm gas}$. The calculations stop at the edge of the H II region where the electron fraction is 10^{-2}. The output emission-line fluxes are normalized by the Hβ line fluxes.

4. Results

4.1. Morphology, Colors, and Optical [O III] Line Map

B14-65666 consists of two bright components: galaxies E (east) and W (west), which were referred to as the clumps A and B in T. Hashimoto et al. (2019), respectively. T. Hashimoto et al. (2019) reported that these two galaxies have similar UV, IR, [O III] 88 μm, and [C II] 158 μm luminosities within a factor of 2 and their line-of-sight velocity separation is $\simeq$200 km s^{-1}. For these reasons, B14-65666 is thought to be a major merger at $z = 7.1520$. The NIRCam observations provide us with morphological evidence for the scenario of the major merger. Figure 1 shows the NIRCam-band color image and the individual images in the six NIRCam filters of the two galaxies of B14-65666. The two galaxies are apparently separated in the rest-frame optical wavelengths, ruling out a scenario that the two bright components are star-forming regions in a rotating stellar disk.

The NIRCam imaging clearly illustrates that galaxies E and W have different morphology. Galaxy E has a bright compact core. This compact core is unresolved even in the F115W image, which has the highest angular resolution in the images used in this work. Under the assumption that the core of galaxy E has an exponential surface brightness profile, the deconvolved effective radius in F115W is $r_{\rm e} < 0\farcs016$ (85 pc) at the 2σ significance limit. This core effective radius is smaller than the average effective radii (0.7–1 kpc at rest-frame optical) of observed and simulated galaxies at $M_* \sim 10^9 M_\odot$ at $z = 7$ (L. Costantin et al. 2023; K. Ormerod et al. 2024).

In contrast, galaxy W is elongated from southeast to northwest. This feature is seen in all the NIRCam images and its length is $\simeq 0\farcs3$ (1.5 kpc). Such elongated morphology looks like tidal tails and it is often observed under tidal effects like major mergers in the local Universe (e.g., K. D. Borne et al. 2000; M. García-Marín et al. 2009). In addition, the F115W and F150W images suggest a clumpy internal structure of galaxy W, which may consist of three clumps. This compactness and clumpiness of B14-65666 agree with rest-frame UV clumps in bright high-redshift galaxies revealed by recent JWST observations (e.g., T. Treu et al. 2023; J. A. A. Trussler et al. 2023; R. Marques-Chaves et al. 2024) and numerical simulations (e.g., N. Mandelker et al. 2017; D. Ceverino et al. 2023; Y. Nakazato et al. 2024).

In addition to the compact and clumpy structure, the NIRCam images have identified some extended emission around galaxy E. This emission is clearly seen in the F444W image and consists of two diffuse subcomponents north and southeast of galaxy E (Figure 1). Actually, the spatially extended components were already suggested in the HST F140W image (R. A. A. Bowler et al. 2017) and the [O III] 88 μm line map (T. Hashimoto et al. 2019), but they were not explicitly reported in the literature due to low S/N. In the NIRCam imaging, the diffuse components are confirmed at $S/N > 6$ in the F277W, F356W, and F444W bands and they are also suggested at lower significance levels ($S/N \simeq 1$–2) in the F150W and F200W images. The F444W bandpass includes Hβ and [O III] $\lambda\lambda$4960,5008 emission lines. The F277W bandpass samples shorter wavelengths than the Balmer break, at which the stellar continuum by old stars becomes faint. Therefore, these multiple band detections imply that the diffuse subcomponents are bright in young stellar continuum or nebular emission (e.g., the [O III] and [O II] $\lambda\lambda$3727,3730 lines and nebular continuum). Given that B14-65666 is a major merging system, we assumed that they are likely to be tidal tails stripped from the galaxies (e.g., M. García-Marín et al. 2009).

Table 2 lists the measured photometry of the total and galaxies E and W. The table also lists the photometry of the tails (N-tail and S-tail) and the cores of galaxies E and W (E-core and W-core). The applied apertures are shown in the left panel of Figure 2. Our measurements of the total photometry are consistent with the values on the COSMOS2020 catalog (*J*, *H*, and *Ks* bands in UltraVISTA and Ch1 and 2 in Spitzer; J. R. Weaver et al. 2022). The F115W magnitudes of galaxies E and W are measured to be $25.9^{+0.5}_{-0.3}$ and $25.5^{+0.2}_{-0.2}$ mag, respectively, corresponding to $M_{\rm UV} = -21.1^{+0.5}_{-0.3}$ and $-21.5^{+0.2}_{-0.2}$ mag. These magnitudes are similar to and brighter than the characteristic magnitude, $M^{*}_{\rm UV} \simeq -21.0$ mag, of the UV luminosity function at $z \sim 7$ (e.g., S. L. Finkelstein et al. 2015; R. J. Bouwens et al. 2021). From UV to optical wavelengths, galaxy E has a redder color than galaxy W. The tails largely contribute to this red color of galaxy E, as shown in Figure 1-. This color difference suggests that galaxies E and W have different stellar and dust properties.

A characteristic color index is the F444W excess, which is twice as high as the F356W flux. This excess corresponds to the [O III] $\lambda\lambda$4960,5008 emission-line strength. While the Hβ line contributes to the F356W flux, both Hβ and [O III] 4960,5008 lines increase the flux measured in the F444W filter. The filter transmission of the Hβ line is similar in both of the bands, 37% (F356W) and 50% (F444W). Therefore, by assuming a constant continuum flux density between F356W and F444W, we created an optical [O III] line map from the F356W − F444W color with little contamination of Hβ emission. Other emission lines of Hγ, Hδ, and [O III] 4363 Å may lead to underestimation of the [O III] flux by 8%–15%, according to CLOUDY calculations at $0.1 < Z_{\rm gas}/Z_{\odot} < 0.4$ and $-1.5 < \log U < -2.5$. A possible red continuum slope would reduce $\simeq$10% of the [O III] line flux and $\simeq$20% of the [O III] equivalent width per the F356W − F444W color of 0.1 mag.

The middle panel of Figure 2 shows the optical [O III] line map, which indicates strong [O III] emission at the cores. The E-core and W-core exhibit integrated [O III] fluxes of $(4.3 \pm 0.4) \times 10^{-17}$ and $(2.0 \pm 0.3) \times 10^{-17}$ erg s^{-1} cm^{-2}, respectively. Being regarded as a proxy of star formation, this strong [O III] emission indicates nuclear starbursts likely induced by the galaxy interaction, as seen in major mergers in the local Universe (e.g., S. L. Ellison et al. 2008). The right panel of Figure 2 shows a map of the rest-frame [O III] equivalent width (EW$_0$). The E-core and W-core exhibit EW$_0$([O III]) $\sim 2050 \pm 290$ and 740 ± 170 Å, respectively, which are at the higher end of the distribution of [O III] emitters at $z = 5$–7 (J. Matthee et al. 2023; K. Boyett et al. 2024). In the tails, the [O III] fluxes are detected at the 3–4σ significance levels, although this value may be overestimated because their red color may reflect their red optical continuum slopes, which is different from our assumption. The obtained [O III] fluxes and equivalent widths are listed in Table 3.

4.2. NIRCam and ALMA Imaging: Stellar Versus Dust Distribution

The combination of the new NIRCam images with archival high-angular-resolution (<0$''$.4) ALMA data provides us with a unique opportunity to investigate the detailed stellar, ionized, and dust structure in an interacting system at $z > 7$. Figure 3 compares the NIRCam image, and ALMA line and dust maps. The NIRCam image is a composite of all the bands, except for F444W, to exhibit the stellar continuum. All the ALMA detections overlap the positions of galaxies E and W, showing no spatial offsets between the UV-to-optical and FIR dust and line emission. The [C II] 158 μm and [O III] 88 μm emission lines in galaxy E are 1–1.5 times as bright as those in galaxy W (T. Hashimoto et al. 2019). This trend is qualitatively the same as the one seen in our [O III] $\lambda\lambda$4960,5008 line map (Table 3). In contrast to the emission lines, the dust emission at 88 and 158 μm is brighter in galaxy W than in galaxy E (T. Hashimoto et al. 2019).[21] This dust spatial distribution might indicate that galaxy W experiences dustier star formation than galaxy E. As denoted in Section 4.1, however, galaxy W presents a bluer UV color than galaxy E, which is inconsistent with a previous finding that dust emission tends to be accompanied by red components in $z > 6$ galaxies (R. A. A. Bowler et al. 2022). We will come back to this point in Section 5.1.

The tails are detected only in the [O III] 88 μm line map, whereas they appear neither in the [C II] 158 μm line map nor in the dust maps. NIRCam detects the tails in the stacked continuum image, generated using the bands from F115W to F356W, and the [O III] $\lambda\lambda$4960,5008 line map. However, the tails are faint in the rest-frame UV filters (e.g., F150W), indicating a red continuum slope from UV to optical. The presence of continuum and line emission implies that the tails are actively forming stars, but the red continuum slope and the no emission of dust continua suggest a complex nature of the tails.

---

[21] The peak position of the 158 μm dust emission is shifted to the east of galaxy W beyond the ideal astrometric uncertainty (Section 2.2). The origin of this shift is unclear, but it might be ALMA astrometric uncertainties poorer than the ideal one.

Table 2

NIRCam Photometry and ALMA Measurements of B14-65666 Components

Aperture	F115W (μJy)	F150W (μJy)	F200W (μJy)	F277W (μJy)	F356W (μJy)	F444W (μJy)	Band 8[a] (μJy)	Band 7[b] (μJy)	Band 6[a] (μJy)	[O III] 88[b] (Jy km s^{-1})
Total	0.374 ± 0.100	0.447 ± 0.043	0.429 ± 0.112	0.661 ± 0.047	0.705 ± 0.046	1.346 ± 0.070	470 ± 128	218 ± 19	130 ± 25	1.50 ± 0.18
E	0.159 ± 0.060	0.162 ± 0.023	0.261 ± 0.051	0.343 ± 0.027	0.355 ± 0.024	0.773 ± 0.040	208 ± 83	…	41 ± 23	0.92 ± 0.14
W	0.225 ± 0.045	0.298 ± 0.019	0.187 ± 0.040	0.298 ± 0.022	0.305 ± 0.020	0.496 ± 0.026	246 ± 73	…	87 ± 26	0.57 ± 0.09
E-core	0.107 ± 0.022	0.128 ± 0.008	0.163 ± 0.018	0.180 ± 0.011	0.167 ± 0.010	0.440 ± 0.022	…	…	…	…
W-core	0.203 ± 0.023	0.232 ± 0.013	0.186 ± 0.019	0.215 ± 0.013	0.220 ± 0.012	0.349 ± 0.018	…	…	…	…
N-tail	0.042 ± 0.025	0.016 ± 0.007	0.042 ± 0.020	0.057 ± 0.009	0.080 ± 0.009	0.116 ± 0.008	…	…	…	…
S-tail	−0.005 ± 0.038	0.014 ± 0.011	0.050 ± 0.033	0.091 ± 0.014	0.091 ± 0.011	0.161 ± 0.011	…	…	…	…

Notes.

[a] T. Hashimoto et al. (2019).

[b] Y. Sugahara et al. (2021).

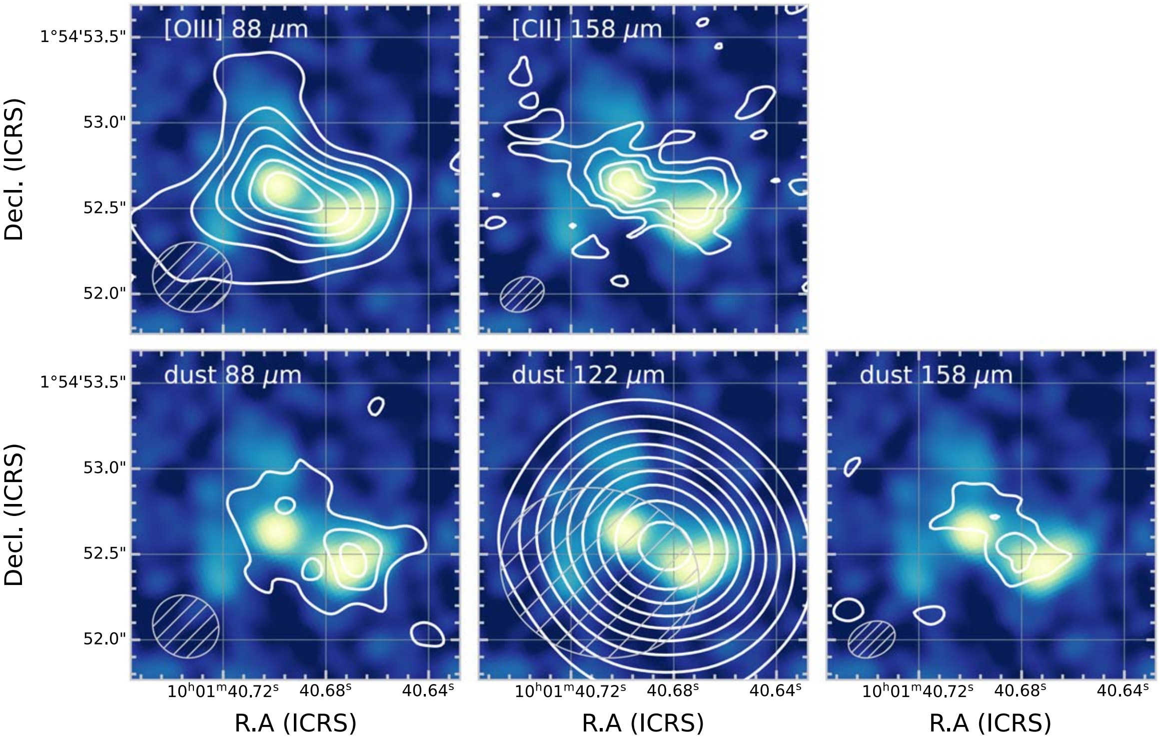

Figure 3. ALMA line and dust contours overlaid on the background NIRCam image. The NIRCam image is a stack of F115W to F356W bands to trace the continuum light, which is homogenized to the F444W PSF. The white contours are drawn with 2σ intervals from the 2σ level, where $\sigma = 0.04$ and 0.02 Jy beam^{-1} km s^{-1} for the [O III] and [C II] line maps and $\sigma = 30$ and 8 μJy beam^{-1} for the 88 and 158 μm dust maps, respectively. For the 122 μm dust map, the white contours are drawn from the 4σ level, where $\sigma = 9\mu$Jy beam^{-1}. The gray hatched ellipses at the left bottom corners are the synthesized beam sizes of ALMA observations.

Table 3
Observed and Physical Properties of Components

Components	Aperture Diameter (arcsec^2)	Flux([O III]) (10^{-17} erg s^{-1} cm^{-2})	EW$_0$([O III]) (Å)	SFR$_0$ ($M_\odot$ yr^{-1})	sSFR$_0$ (Gyr^{-1})	SFR$_{10\ \mathrm{Myr}}$ ($M_\odot$ yr^{-1})	β_{UV}
Total	1.8 × 1.8	10.1 ± 1.3	1140 ± 220	225^{+71}_{-56}	52^{+56}_{-28}	207^{+65}_{-51}	$-1.57^{+0.11}_{-0.13}$
E	1.4 × 0.80	6.6 ± 0.7	1480 ± 260	178^{+52}_{-39}	53^{+26}_{-20}	178^{+50}_{-39}	$-1.18^{+0.15}_{-0.16}$
W	1.1 × 0.66	2.6 ± 0.4	750 ± 170	37^{+12}_{-8}	23^{+15}_{-11}	37^{+12}_{-8}	$-2.19^{+0.11}_{-0.09}$
E-core	0.44 × 0.44	4.3 ± 0.4	2050 ± 290	180^{+113}_{-58}	506^{+253}_{-182}	34^{+13}_{-9}	$-1.78^{+0.11}_{-0.13}$
W-core	0.44 × 0.44	2.0 ± 0.3	740 ± 170	29^{+13}_{-7}	27^{+28}_{-12}	29^{+14}_{-6}	$-2.24^{+0.13}_{-0.10}$
N-tail	0.70 × 0.40	0.6 ± 0.2	580 ± 260	…	…	…	…
S-tail	1.0 × 0.50	1.1 ± 0.2	960 ± 340	…	…	…	…

Note. The flux([O III]) and EW$_0$([O III]) are the line fluxes and rest-frame equivalent widths derived from the optical [O III] $\lambda\lambda$4960,5008 line map (Figure 2) within the component apertures. SFR$_0$ is the instant star formation rate ($\mathrm{SFR}_0 = M_*/t_{\mathrm{SF}}$) and SFR$_{10\ \mathrm{Myr}}$ is the star formation rate averaged in 10 Myr, that is, $\mathrm{SFR}_{10\ \mathrm{Myr}} = M_*(<10\ \mathrm{Myr})/10\ \mathrm{Myr}$. The specific SFR$_0$ is defined as $1/t_{\mathrm{SF}}$. β_{UV} is the UV spectral slope.

4.3. SED Fitting of Total and Resolved Components

We performed SED fitting combining the NIRCam and ALMA data sets for the entire system and the resolved galaxy components of B14-65666. The apertures for each component are illustrated in the left panel of Figure 2 and the NIRCam and ALMA fluxes used in the SED fitting are summarized in Table 2. The best-fit SEDs and measured physical parameters are presented in Figure 4 and Table 4, respectively. The best-fit parameters are given as 2σ upper/lower limits when the peak of the posterior distributions is near the edge of the parameter boundaries (see the Appendix).

4.3.1. Entire Merging System

The SED fit to the integrated flux supports that the B14-65666 system is a young starburst, regardless of whether including the ALMA data. In the case without the ALMA data, the star formation age and the stellar mass are $t_{\mathrm{SF}} = 20^{+20}_{-10}$ Myr and $\log M_*/M_\odot = 9.6^{+0.3}_{-0.3}$, and then, instant SFR is $\mathrm{SFR}_0 = M_*/t_{\mathrm{SF}} = 230^{+70}_{-60} M_\odot\ \mathrm{yr}^{-1}$. The ionization parameter is $\log U = -2.1^{+0.5}_{-0.3}$. This young starburst with the high ionization parameter gives rise to strong [O III] emission lines that can explain the F444W excess. The relatively red stellar continuum even with the young starburst is attributed to the dust attenuation of $A_{\mathrm{V}} = 0.86^{+0.1}_{-0.1}$ mag. The old stellar component is constrained to be $\log M_*/M_\odot < 9.7$ at the 2σ upper limit, which contributes to the estimated continuum at F444W by up to 10%. This upper limit is comparable to the stellar mass formed by the present star formation. Thus, the starburst induced by the major merger formed a stellar mass comparable to or higher than the old stellar mass built before the ongoing merger.

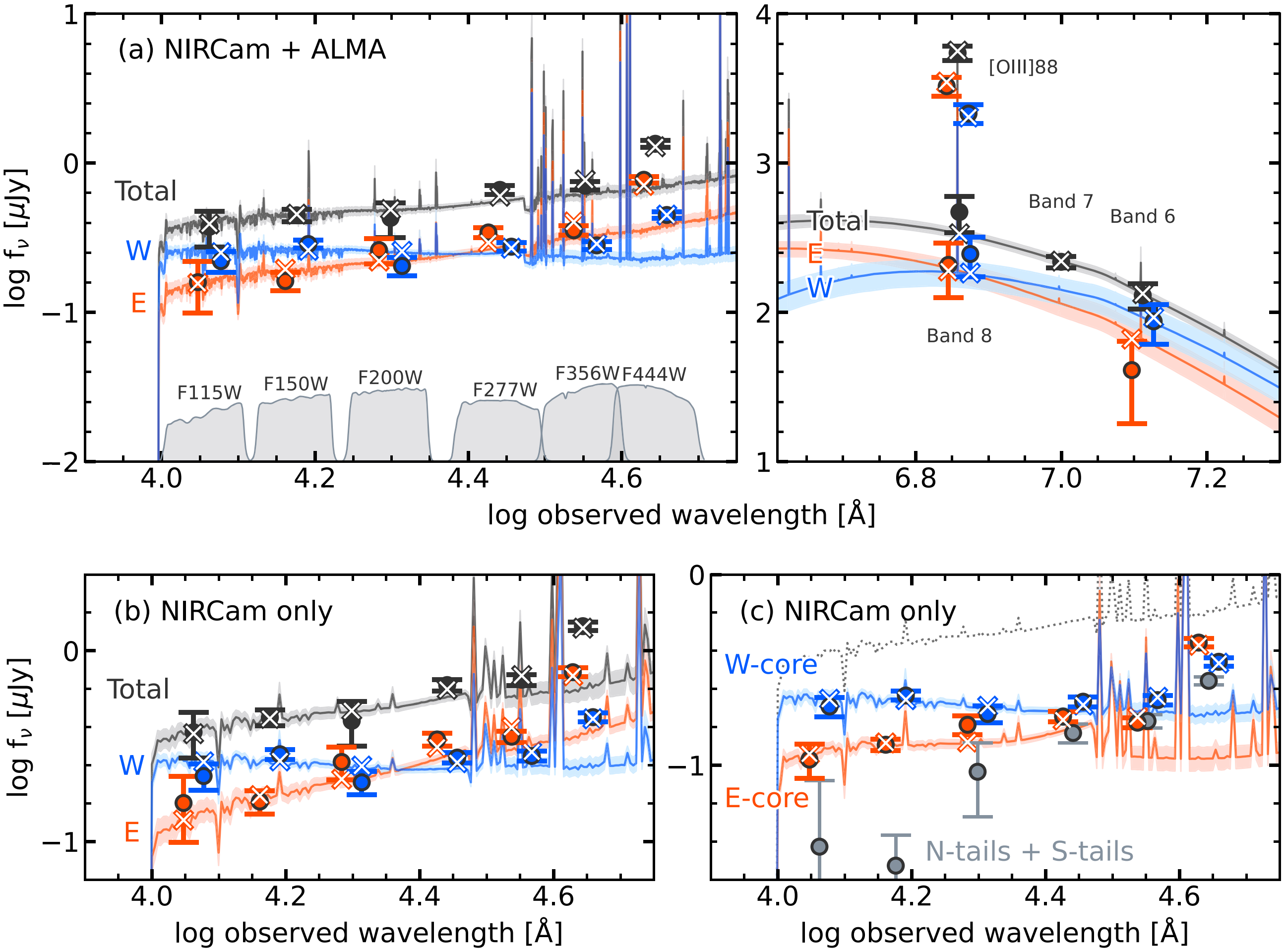

Figure 4. SEDs of B14-65666 and the results of the SED fitting. (a) SED fitting results for the NIRCam and ALMA measurements. Each color shows the data of each component: total (black) and galaxies E (red) and W (blue). The circles indicate the measured photometry and the error bars indicate the measurement errors including the absolute flux uncertainties. The data points are shifted from the centers of the filters for illustration purposes. The crosses show the obtained best-fit photometry of the SED fitting. The solid lines and shades show the best-fit curves and uncertainties taking 16–84 percentiles of the posterior distributions. The bottom gray shades of the left panel show the transmission curves of the NIRCam filters. (b) SED fitting results only for the NIRCam photometry, without ALMA measurements. The best-fit parameters are comparable to the ones obtained for the NIRCam and ALMA measurements (Table 4). (c) SED of the E-core (red) and W-core (blue) and the obtained best-fit results for them. The gray data points show the SED of the tails, which is the sum of the N-tail and S-tail. The dotted line is shown for comparison, which is the same as the black line in panel (b).

Table 4
Results of SED Fitting

Components	$t_{\rm SF}$ (Myr)	$\log M_*$ ($\log M_\odot$)	$A_{\rm V}$ (mag(AB))	$\log U$	Z_* ($Z_\odot$)	$\log M_{\rm old}$ ($\log M_\odot$)	$\mathcal{U}_{\rm min}$	γ
NIRCam + ALMA data[a]								
Total	35^{+20}_{-12}	$9.78^{+0.16}_{-0.18}$	$0.78^{+0.07}_{-0.06}$	$-2.09^{+0.58}_{-0.34}$	$0.21^{+0.05}_{-0.04}$	<9.59	>10.45	$0.88^{+0.07}_{-0.07}$
E	<93	$9.55^{+0.19}_{-0.20}$	$0.98^{+0.08}_{-0.07}$	$-2.06^{+0.61}_{-0.34}$	$0.19^{+0.04}_{-0.04}$	<9.55	>16.33	>0.83
W	22^{+13}_{-8}	$9.09^{+0.16}_{-0.18}$	$0.46^{+0.08}_{-0.06}$	$-1.95^{+0.54}_{-0.39}$	$0.32^{+0.06}_{-0.05}$	<8.95	>7.61	<0.80
Only NIRCam data[b]								
Total	18^{+21}_{-9}	$9.61^{+0.25}_{-0.27}$	$0.86^{+0.11}_{-0.11}$	$-2.14^{+0.47}_{-0.34}$	$0.26^{+0.09}_{-0.08}$	<9.68	⋯	⋯
E	<53	$9.51^{+0.17}_{-0.14}$	$1.21^{+0.13}_{-0.14}$	$-2.19^{+0.42}_{-0.30}$	$0.28^{+0.09}_{-0.08}$	<9.28	⋯	⋯
W	42^{+39}_{-17}	$9.22^{+0.17}_{-0.17}$	$0.34^{+0.12}_{-0.09}$	$-2.08^{+0.54}_{-0.37}$	$0.24^{+0.09}_{-0.08}$	<8.95	⋯	⋯
E-core	<5	$8.53^{+0.15}_{-0.13}$	$0.72^{+0.15}_{-0.14}$	$-1.82^{+0.49}_{-0.29}$	$0.33^{+0.11}_{-0.10}$	<8.87	⋯	⋯
W-core	35^{+29}_{-18}	$9.02^{+0.19}_{-0.20}$	$0.30^{+0.14}_{-0.10}$	$-1.99^{+0.67}_{-0.38}$	$0.26^{+0.10}_{-0.10}$	<8.89	⋯	⋯

Notes. The fitting parameters are described in Section 3.2. The best-fit values and 1σ uncertainties are computed from the 50 percentile and 16 and 84 percentiles of the posterior distributions, respectively. The upper and lower limits are the 2σ limits, that is, 97.5 and 2.5 percentiles of the posterior distributions, respectively.

[a] The results for the NIRCam and ALMA photometry.

[b] The results are only for the NIRCam photometry. The dust emission parameters $\mathcal{U}_{\rm min}$ and γ are not used in the fits.

The SED fitting including the dust continua shows higher $\mathcal{U}_{\rm min}$ and γ values than those of nearby galaxies ($\mathcal{U}_{\rm min} \lesssim 10$ and $\gamma \lesssim 0.1$ in B. T. Draine & A. Li 2007). Such high $\mathcal{U}_{\rm min}$ and γ were also obtained for UV-selected galaxies at $z > 4.5$ (D. Burgarella et al. 2022), indicating the necessity of high dust temperature to explain the FIR dust emission in high-redshift galaxies. The characteristic dust temperature,[22] derived from Equation (33) in B. T. Draine & A. Li (2007) and Equation (13) in B. T. Draine et al. (2014), is $T_{\rm d,\,char} \simeq 18\langle \mathcal{U} \rangle^{1/6}\ K = 48^{+2}_{-3}$ K, which is consistent with the dust temperature obtained from the modified blackbody fitting (Y. Sugahara et al. 2021). Although including the ALMA data slightly decreases the uncertainties of the best-fit dust attenuation and stellar metallicity, the changes in the best-fit stellar properties are insignificant.

Previous analyses of the entire properties of B14-65666 yielded stellar masses that are less than one-third of the one presented in this work (R. A. A. Bowler et al. 2018; T. Hashimoto et al. 2019). On the other hand, the instant SFR_0 that they obtained is consistent with our estimate (T. Hashimoto et al. 2019). The stellar mass discrepancy is because of the differences in the IRAC and NIRCam photometry, where IRAC flux densities were 1.5–2 times as low as the NIRCam flux densities at 3.6 and 4.4 μm. We note again that our new photometry agrees with that in the COSMOS2020 catalog, which is also higher than the previous photometry at 3.6 μm and 4.5 μm.

4.3.2. Resolved Components

The high angular resolution of the NIRCam imaging enables us to perform the SED fitting to each of the galaxy components. Figure 4 makes it clear that galaxies E and W have different colors in the rest-frame UV-to-optical wavelengths. In the cases without the ALMA data, they are inferred as the young starbursts with ages of <53 Myr and 40^{+40}_{-20} Myr, respectively, similar to the total. The $\mathrm{SFR}_{10\ \rm Myr}(= M_*(<10\ \mathrm{Myr})/10\ \mathrm{Myr})$ of galaxy E ($180^{+50}_{-40} M_\odot\ \mathrm{yr}^{-1}$) is $\simeq$4 times as high as that of galaxy W ($40^{+10}_{-10} M_\odot\ \mathrm{yr}^{-1}$). Moreover, galaxy E is expected to have $\gtrsim$0.5 mag stronger dust attenuation than galaxy W. These results reflect a dusty, bursty phase of galaxy E, which is also supported by the strong F444W excess, i.e., the highest [O III] line strength at the core of galaxy E (Section 4.1). In the SED fitting including the ALMA data, the [O III] 88 μm emission-line fluxes help more strictly constrain the metallicity of the galaxies; galaxy E exhibits a lower stellar metallicity than galaxy W while they have a similar metallicity in the SED fitting without the ALMA data. These metallicity constraints originate from better constraints on the gas-phase metallicity by the optical-to-FIR [O III] line ratios. Both of the galaxies show small Balmer jumps (or inverse Balmer break), a flux excess at wavelengths shorter than 4000 Å caused by the nebular continuum, which is especially strong for galaxy E. The contribution of this nebular continuum and [O II] $\lambda\lambda$3727,3730 emission lines help to boost the F277W flux at a level similar to that of the F356W filter. The sum of the stellar masses of the galaxies is $\log M_*/M_\odot \simeq 9.68$, which is comparable to the stellar mass derived from the total photometry. We note that the old stellar component ($M_{\rm old}$), which is frequently missed in modeling only with young starburst populations (G. W. Roberts-Borsani et al. 2020; C. Giménez-Arteaga et al. 2023), may contribute up to a factor of 2 to the total stellar mass as discussed in the previous section. Finally, the stellar-mass ratio of galaxies E and W is estimated to be 3:1 to 2:1. This mass ratio is comparable to the dynamical mass ratio of galaxy E ($5.7 \pm 1.6 \times 10^{10} M_\odot$) to galaxy W ($3.1 \pm 1.1 \times 10^{10} M_\odot$) that are inferred from the [O III] 88 μm line widths on the assumption of the virial theorem (T. Hashimoto et al. 2019). Thus, this study has revealed that B14-65666 is surely a major merger in terms of the stellar mass ratio of the galaxies, while previous studies identified it from the luminosity ratio.

In the FIR SED, it is notable that galaxies E and W have different peaks of the dust continua. The NIRCam and ALMA observations have shown that galaxy E has a redder UV spectral slope while galaxy W exhibits higher dust-continuum flux densities. The SED fitting explains these observations with a difference in the dust temperatures. In particular, galaxy E requires so high $\mathcal{U}_{\rm min}$ and γ that their probability distribution functions reach the maximum values of their permitted parameter ranges. The characteristic dust temperatures are $T_{\rm d,\,char} = 50^{+1}_{-2}$ and 40^{+4}_{-3} K for galaxies E and W, respectively. We will further discuss the relations between the UV and FIR light in Section 5.1.

For finer resolved analyses, we divided the system into the cores of the galaxies and the tails in galaxy E. We did not include the ALMA data in these SED fittings, which have relatively lower angular resolution. Panel (c) of Figure 4 depicts the observed SED and best-fit spectra for the E-core and W-core. The W-core has a similar SED shape to galaxy W and is 10%–30% fainter than it; this similarity means that the W-core is dominant in the SED of galaxy W. On the other hand, the E-core is twice as faint as galaxy E at the long wavelength channels. The obtained best-fit age is very young, $<$5 Myr, at the 2σ upper limit and the stellar mass is $\simeq$1.0 dex lower than that of galaxy E. As shown in panels (b) and (c), there is a $>$0.4 dex difference in the best-fit stellar continua at wavelengths longer than the Balmer jump. These differences indicate that the red tails strongly affect the SED of galaxy E at the rest-frame optical wavelengths. One possible scenario to interpret this result might be that galaxy E is composed of the dusty compact starbursts at the nucleus and the older stars in the tails which dominate the stellar mass. However, the nondetections in the F115W, F150W, and F200W bands of the tails make it challenging to understand the origin of their red color by solving the degeneracy between the old stellar populations, dust attenuation, and strong emission lines (Figure 4). Detailed properties of the tails will be estimated by including emission lines taken in approved JWST NIRSpec and MIRI observations.

5. Discussion

5.1. IRX–β_{UV} Relation

The NIRCam and ALMA data presented so far have demonstrated the complex structure of stellar and interstellar-medium properties in the system B14-65666. While galaxy W is bluer than galaxy E in the rest-frame UV (Figure 4), it exhibits brighter dust emission (Figure 3). This originates from different properties of star formation and dust attenuation between galaxies E and W. The SED fitting in Section 4.3 has suggested the different dust temperatures as the origin, but there are other physical mechanisms including assumptions of the dust attenuation curve.

We investigate the relation between the IR excess ($\mathrm{IRX} = L_{\rm IR}/L_{\rm UV}$) and the UV spectral slope $\beta_{\rm UV}$ to study

---

[22] Within the given fitting parameter ranges of $\mathcal{U}_{\rm min}$ and γ, the maximum characteristic temperature is 52.4 K.

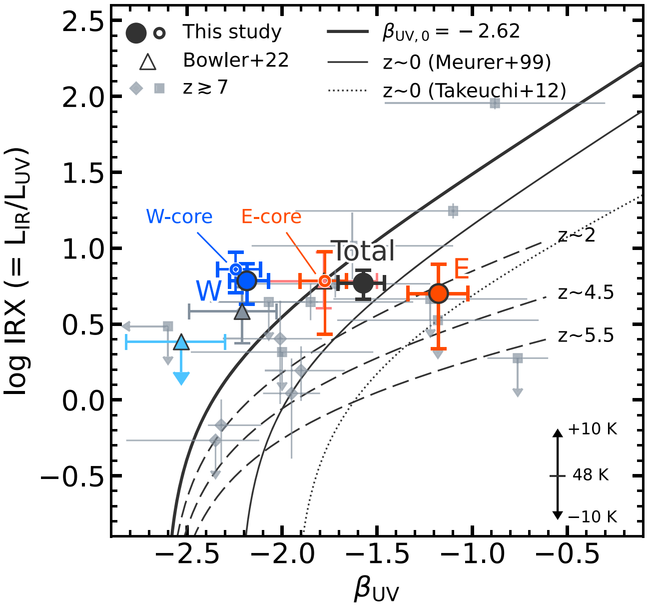

Figure 5. IRX–$\beta_{\rm UV}$ diagram. The black, red, and blue circles show the measurements for the total, galaxy E, and galaxy W of B14-65666. The E-core and W-core are depicted with small circles with the same colors as those of galaxies E and W, respectively. The light-color triangles show the measurements for B14-65666 obtained by R. A. A. Bowler et al. (2022). We note that the galaxy E symbol of Bowler et al. is completely overlapped with our E-core symbol. The small gray symbols show $z \sim 7$ galaxies taken from R. A. A. Bowler et al. (2022, diamond) and T. Hashimoto et al. (2019, square). All the IRX values of the data points from the literature are corrected for $T_{\rm d} = 48$ K and $\beta_{\rm d} = 2.0$. The lines show the parameterized IRX–$\beta_{\rm UV}$ relations: the black solid line is the G. R. Meurer et al. (1999) relation modified with $\beta_{\rm UV,0} = -2.62$ (N. A. Reddy et al. 2018), the thin solid line is the original Meurer relation ($\beta_{\rm UV,0} = -2.23$) for UV-selected local starbursts, the dotted line is an aperture-corrected Meurer relation (T. T. Takeuchi et al. 2012), and the dashed lines are relations obtained for UV-selected galaxies at $z \sim 2$ (N. A. Reddy et al. 2018) and $z \sim 4.5$ and 5.5 (Y. Fudamoto et al. 2020). The bottom right arrows show how the IRX values change if the assumed dust temperature increases or decreases from 48 K.

whether the discrepancy between the UV colors and dust emission is due to the dust attenuation curve. We computed the monochromatic rest-frame UV luminosity $L_{\rm UV}$ and $\beta_{\rm UV}$ from the best-fit SED models derived without the ALMA data. The UV luminosity was computed from the UV continuum as $L_{\rm UV} = \lambda L_\lambda$ at $\lambda = 1600$ Å. The UV slope was obtained by linear fitting to the UV continuum within the wavelength windows proposed by D. Calzetti et al. (1994). The measurement uncertainties were propagated from the fitting uncertainties; we measured values from the 500 SED models derived from the parameter posterior distributions and estimated uncertainties from the measurement distribution. The IR luminosity $L_{\rm IR}$ was taken from T. Hashimoto et al. (2019), who estimated it by the modified blackbody fitting under the assumption of the dust temperature of $T_{\rm d} = 48$ K and the dust emissivity of $\beta_{\rm d} = 2.0$. This assumed dust temperature agrees with the characteristic dust temperature $T_{\rm d,\ char}$ of the entire system that has been derived in the SED fitting.

The obtained IRX values of the entire system (total) and both of the galaxies are similar, $\log {\rm IRX} \simeq 0.7$. However, the $\beta_{\rm UV}$ values range from $\beta_{\rm UV} = -2.2$ (galaxy W) to -1.2 (galaxy E). The UV slope $\beta_{\rm UV}$ depends on stellar and dust properties including age, dust composition, and the stellar-and-dust geometry. Therefore, the variation in $\beta_{\rm UV}$ at a given IRX supports a spatial variation of stellar and dust properties between the components.

Previously R. A. A. Bowler et al. (2022) measured the IRX and $\beta_{\rm UV}$ values for B14-65666. In Figure 5, we plotted their data points after correcting the IRX values for $T_{\rm d} = 48$ K and $\beta_{\rm d} = 2.0$. Compared with their values, our measurements are systematically redder in $\beta_{\rm UV}$. Although the origin of the systematics is unclear, the $\beta_{\rm UV}$ difference would be caused by different spatial resolutions. R. A. A. Bowler et al. (2022) used UltraVISTA images with spatial resolutions of $\sim 0\farcs7$, much coarser than those of our NIRCam images, and they resolved objects with `TPHOT` (E. Merlin et al. 2015) based on an HST image. Thus, unexpected systematics may be included in their rest-frame UV photometry. This comparison underlines the power of high resolution for spatially resolved studies.

The IRX–$\beta_{\rm UV}$ relations are connected with attenuation curves under the energy balance between absorption and reradiation by dust (G. R. Meurer et al. 1999). Canonical relations are parameterized with attenuation curves, for example, for local starbursts (G. R. Meurer et al. 1999; R. A. Overzier et al. 2011; T. T. Takeuchi et al. 2012) and for the Small Magellanic Cloud (SMC; M. L. Prevot et al. 1984; K. D. Gordon et al. 2003). For high-redshift galaxies, the intrinsic UV slope, $\beta_{\rm UV,0}$, is bluer than that for the local starbursts (N. A. Reddy et al. 2018) due to the young ages, low stellar metallicities, and binary interactions (C. C. Steidel et al. 2014, 2016), although the nebular-continuum emission could make it redder. We checked $\beta_{\rm UV,0}$ of our best-fit intrinsic SED curves before dust reddening and found that it ranges from $\beta_{\rm UV,0} = -2.6$ to -2.55, which is bluer than -2.23 used in G. R. Meurer et al. (1999). For simplicity, we use $\beta_{\rm UV,0} = -2.62$ (N. A. Reddy et al. 2018) as a fiducial value at high redshift.

Figure 5 compares the measurements for B14-65666 and various IRX–$\beta_{\rm UV}$ relations. The total is in good agreement with the widely used canonical relation, the G. R. Meurer et al. (1999) relation, modified to $\beta_{\rm UV,0} = -2.62$. From this result, (1) the agreement with the Meurer relation supports our assumption of using the D. Calzetti et al. (2000) attenuation curve in the SED fitting and (2) $\beta_{\rm UV,0} = -2.62$ supports lower stellar metallicity and younger ages of B14-65666 than those of local starbursts (G. R. Meurer et al. 1999; R. A. Overzier et al. 2011; T. T. Takeuchi et al. 2012). Galaxies E and W are, however, not consistent with the $\beta_{\rm UV,0}$-modified Meurer relation. Galaxies E and W exhibit lower and higher IRX than the relation at their $\beta_{\rm UV}$, respectively. Deviations from the canonical IRX–$\beta_{\rm UV}$ relations arise from several physical processes (e.g., G. Popping et al. 2017). For galaxy E, the low IRX value would be explained by hypotheses that galaxy E has higher dust temperatures of $T_{\rm d} \geqslant 63$–68 K in the modified blackbody, as suggested by the SED fitting (Section 4.3.2); or that galaxy E exhibits a steeper SMC-like dust attenuation curve than the D. Calzetti et al. (2000) one. Alternatively, the measurement of $\beta_{\rm UV}$ based on the SED fitting may be affected by the red tails. If we assume that the measured dust emission only arises from the E-core, the E-core is located on the $\beta_{\rm UV,0}$-modified Meurer relation on the IRX–$\beta_{\rm UV}$ diagram. For galaxy W, hypotheses to explain the IRX values are a low dust temperature of $T_{\rm d} \leqslant 27$–33 K, which qualitatively agrees with the SED fitting result; or the patchy stellar-and-dust geometry unresolved even with NIRCam and ALMA ($\lesssim$0.2–1.5 kpc), which produces flatter dust attenuation curves resulting in high IRX at blue $\beta_{\rm UV}$. The patchy stellar-and-dust geometry has been already found in a Lyman-break galaxy at $z = 8.31$

(Y. Tamura et al. 2023) and supported by the FirstLight simulations, where complex stellar-and-dust geometry produces high IRX (M. Mushtaq et al. 2023). In any scenario, or a combination of several scenarios, our rest-frame UV and FIR observations have highlighted the different dust properties between galaxies E and W.

B14-65666 and most other $z \gtrsim 7$ galaxies (T. Hashimoto et al. 2019; R. A. A. Bowler et al. 2022) are distributed between the Meurer relations with $\beta_{\rm UV,0} = -2.23$ (black thin line in Figure 5) and -2.62 (black thick line). From this distribution, T. Hashimoto et al. (2019) and R. A. A. Bowler et al. (2022) concluded that dust-detected galaxies at $z \gtrsim 7$ follow the D. Calzetti et al. (2000) attenuation curve. The apparent IRX dispersion would be explained by a combination of a $\beta_{\rm UV,0}$ variation (i.e., a variation of stellar age and metallicity) and patchy stellar-and-dust geometry (N. A. Reddy et al. 2018). We note that their IRX is corrected for $T_{\rm d}$ and $\beta_{\rm d}$ used in this study and that their $\beta_{\rm UV}$ was derived from photometry, which is different from our method. These results are consistent with stacking analyses of Lyman-break galaxies at $z \sim 3$ (e.g., J. Álvarez-Márquez et al. 2016, 2019; R. A. A. Bowler et al. 2024), but seem to be inconsistent with steeper attenuation curves favored in stacking analyses of UV-selected galaxies at $z \sim 2$ (N. A. Reddy et al. 2018) and $z \sim 4.5$ and 5.5 (Y. Fudamoto et al. 2020). However, some literature galaxies in Figure 5 have stringent IRX upper limits below the canonical relations at high $\beta_{\rm UV}$ and the IRX estimates significantly depend on the assumptions of $T_{\rm d}$ and $\beta_{\rm d}$ and how to measure $\beta_{\rm UV}$. The "standard" IRX–$\beta_{\rm UV}$ relation at high redshift is still under debate.

5.2. *[O III] Line Ratio: Insights into Gas-phase Metallicity*

NIRCam images have identified a flux excess in the F444W band interpreted as a strong [O III] $\lambda\lambda$4960,5008 emission. The ALMA Band 8 has detected the [O III] 88 μm emission. Due to the large difference in their excitation energy, the ratio of the optical-to-FIR [O III] emission lines is sensitive to the physical conditions (electron density and temperature) of the ionized emitting gas (D. E. Osterbrock & G. J. Ferland 2006). This line ratio also depends on the gas-phase metallicity under the assumptions of photoionization models (e.g., Y. Nakazato et al. 2023). Thus, a combination of the NIRCam images and ALMA moment-0 map provides us with insights into spatial distributions of gas-phase metallicity.

We created a line ratio map by taking a ratio of the optical [O III] $\lambda\lambda$4960,5008 emission-line map to the FIR [O III] 88 μm image. The optical [O III] line map was created as in Section 4.1, but here the F356W and F444W images were corrected for the dust attenuation before creating the line map. We corrected flux densities within the apertures E ($A_{\rm V}$ = 1.2 mag), W (0.34 mag), and E-core (0.72 mag) so that the flux density recovered in each aperture agreed with the best-fit $A_{\rm V}$ value obtained in the SED fitting. The created attenuation-corrected optical line map was convolved to match the angular resolution of the ALMA synthesized beam ($0\farcs38$). The map area is limited to the region where both lines are detected at more than 1σ level and it corresponds to 3–4 beam solid angle.

The top panel of Figure 6 illustrates the optical-to-FIR [O III] line ratio map. The line ratio at the peak of the [O III] 88 μm surface brightness is $\simeq$7.8, and 10.6 $\pm$ 1.9 for the integrated flux, where the error does not include the uncertainty of $A_{\rm V}$. The figure shows the spatial variation in the line ratio over the galaxies, which suggests a variation in the electron temperature and/or electron density in galaxies E and W. At the peak positions of the E-core and W-core, the [O III] line ratios are 9.2 and 5.6, respectively. The highest line ratios are seen in the S-tail; however, these high values are based on the assumed strong dust correction and include large uncertainties.

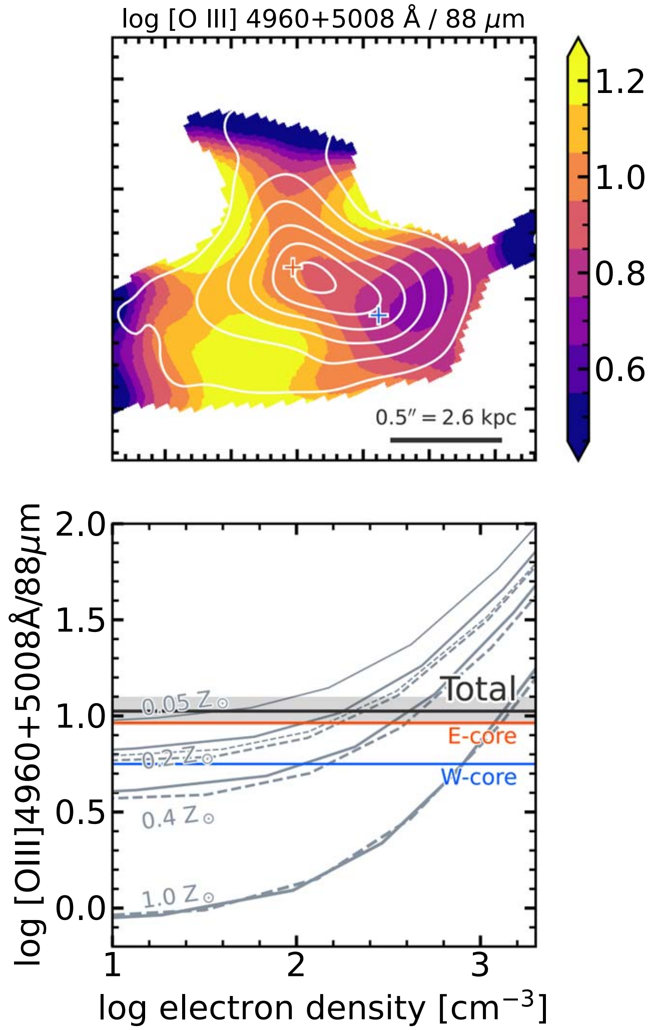

Figure 6. Top: map of the optical-to-FIR [O III] emission-line ratio, color coded by log [O III] 4960 + 5008 Å/[O III] 88 μm. The white contours show the [O III] 88 μm fluxes, which is the same as in Figure 3. The red and blue crosses depict the peak positions of the E-core and W-core, respectively. Bottom: optical-to-FIR [O III] emission-line ratio as a function of the electron density. The horizontal lines show the line ratios of the entire system (black) and the value at the peak positions of the E-core (red) and W-core (blue). The gray curves illustrate theoretical predictions computed from CLOUDY. The line thicknesses depend on the gas-phase metallicity and the solid and dashed lines are at $\log U = -1.5$ and -2.5, respectively. At a typical electron density ($\sim$200 cm^{-3}), the gas-phase metallicity of the B14-65666 is $\simeq 0.2 Z_{\odot}$.

To be more quantitative, we used CLOUDY to explore nebular parameters that reproduce the obtained [O III] line ratios. In our photoionization models, the [O III] line ratio depends on nebular parameters: the gas-phase metallicity $Z_{\rm gas}$, ionization parameter U, and hydrogen density $n_{\rm H}$. As the F356W band includes weak emission lines, which are also subtracted from F444W flux, we corrected the model [O III] $\lambda\lambda$4960,5008 line fluxes by subtracting expected Hγ and Hδ line fluxes. The bottom panel of Figure 6 shows optical-to-FIR [O III] line ratios as a function of the nebular parameters. The illustrated model lines depend on $Z_{\rm gas}$ and U; the low gas-phase metallicity and high ionization parameter increase the electron temperature of the ionized gas, leading to strong [O III] $\lambda\lambda$4960,5008 lines with respect to [O III] 88 μm line. Instead of $n_{\rm H}$ at the illuminated surface, we used the averaged electron density $n_{\rm e}$ for the x-axis that was computed from the modeled [O III] 52 and 88 μm line ratios at the electron temperature of 1.2×10^4 K using PyNeb (V. Luridiana et al. 2015).

The estimated gas-phase metallicity is $Z_{\rm gas} \sim 0.2$–$0.4 Z_\odot$ for the total, at an assumed electron density of $n_{\rm e} \sim 200$–$400\,{\rm cm}^{-3}$, which is a typical estimate from optical-to-FIR [O III] line ratios at high redshift (M. Stiavelli et al. 2023; S. Fujimoto et al. 2024). Using the line ratios at the peak positions of the E-core and W-core, the E-core exhibits a lower gas-phase metallicity of $Z \sim 0.2$–$0.4 Z_\odot$ than the W-core ($> 0.4 Z_\odot$). These results are consistent with conclusions of the previous studies using the [O III] 88 μm emission line that B14-65666 has subsolar metallicity but not extremely low at $<0.1 Z_\odot$ (T. Hashimoto et al. 2019; T. Jones et al. 2020b; S. Yang & A. Lidz 2020). The estimated values here are slightly higher than the metallicities derived from the SED fitting to the NIRCam and ALMA data, reflecting the assumed hydrogen (i.e., electron) density of $n_{\rm H} = 100\,{\rm cm}^{-3}$ in `Bagpipes`. We note that adopting higher electron densities of $n_{\rm e} \sim 600\,{\rm cm}^{-3}$, which is derived from optical emission lines (e.g., Abdurro'uf et al. 2024), results in higher $Z_{\rm gas}$. In terms of the electron density, the optical-to-FIR [O III] line ratios disagree with the presence of a high electron density gas ($n_{\rm e} > 10^4\,{\rm cm}^{-3}$), which have been traced by high-ionization UV emission lines in some high-redshift galaxies (e.g., R. Marques-Chaves et al. 2024; P. Senchyna et al. 2024) under the assumption that galaxies in the EoR would have subsolar metallicity.

5.3. Overall Scenario for the B14-65666 System

The NIRCam and ALMA observations have shed light on the morphology and physical properties of B14-65666 in the EoR. We analyzed the rest-frame optical and FIR data to show the complex morphology of the merging galaxies: galaxy E is composed of a compact core with faint dust emission and diffuse red tails; galaxy W presents an elongated and clumpy morphology with bright dust emission. These clumpy, elongated structures and diffuse-emission-like tidal tails are reproduced in the simulations of high-redshift galaxies ($z = 6$–9, Y. Nakazato et al. 2024). Furthermore, galaxy W may exhibit patchy stellar-and-dust geometry that is not resolved in our observations. These results indicate that B14-65666 is experiencing strong tidal forces accompanied by a merger, disturbing the entire morphology of the system and each of the galaxies involved in the process.

The projected separation of galaxies E and W is $d \simeq 4$ kpc and their line-of-sight velocity difference is $v \simeq 200\,{\rm km\,s}^{-1}$ (T. Hashimoto et al. 2019). Although this is the first-order estimate, the timescale elapsed from the previous passage is estimated to be $d/v \simeq 20$ Myr, which is comparable to the star formation age inferred from the SED fitting. This merging timescale is feasible because it is shorter than the expected merger observability timescale of 180 Myr at $z = 7.15$ (G. F. Snyder et al. 2017). This consistency supports that the gravitational interactions have driven the star formation in B14-65666 after the first (or second) passage.

Major mergers would promote gas accretion by removing the angular momentum from disk gas, triggering starbursts at the cores of the galaxies (e.g., J. C. Mihos & L. Hernquist 1994). B14-65666 shows signatures of nuclear dusty starbursts, including strong optical [O III] emission, strong dust attenuation, and high SFR. These nuclear dusty starbursts have indeed enhanced the star-forming activity of B14-65666. The instant SFR$_0$ of $230\,M_\odot\,{\rm yr}^{-1}$ is $\simeq$1 dex higher than the star formation main sequence at $\log M_*/M_\odot = 9.7$ and $z \sim 7$ (P. Popesso et al. 2023). The merger-induced star formation at high redshift is consistent with a finding in the FirstLight simulations that bursty star formation is induced by gas-rich mergers at $z > 5$ (D. Ceverino et al. 2018). While many observations demonstrate that major mergers enhance SFR in the local Universe (e.g., S. L. Ellison et al. 2008), the SFR enhancement is reported to be inefficient at $z > 1$ (e.g., A. Silva et al. 2018; E. A. Shah et al. 2022). B14-65666 is a clear example of experiencing enhanced star formation at higher redshift.

In particular, the E-core experiences a compact, centrally concentrated, strong starburst. Given $r_{\rm e} < 85$ pc of the E-core in the F115W image and SFR$_0$ values in Table 3, the SFR$_0$ surface density of the E-core is $\Sigma_{\rm SFR,0} \gtrsim 4 \times 10^3 M_\odot\,{\rm yr}^{-1}\,{\rm kpc}^{-2}$, which is comparable to IR SFR surface densities of local ULIRGs or obscured AGN (M. Pereira-Santaella et al. 2021). We expect that this compact starburst is caused by a significant gas accretion to the E-core. The high $\Sigma_{\rm SFR,0}$ is also consistent with the expected high dust temperature of the E-core (see L. Liang et al. 2019). We note that the star formation timescale of the E-core (<5 Myr) is much shorter than those of ULIRGs, as the SFR of ULIRGs is derived from the FIR luminosity (i.e., ~100 Myr). Although the molecular gas mass is highly uncertain for B14-65666 ($10^{8.7-11} M_\odot$, T. Hashimoto et al. 2023b), the high $\Sigma_{\rm SFR,0}$ would lead to short gas depletion time of <10 Myr in the range of molecular gas mass surface densities of local starbursts ($<10^4 M_\odot\,{\rm pc}^{-2}$; J. A. Hodge et al. 2015; M. Pereira-Santaella et al. 2021). In addition, the high $\Sigma_{\rm SFR,0}$ and sSFR$_0$ of the E-core suggest that the radiation pressure is high enough to launch galactic outflows (e.g., M. Pereira-Santaella et al. 2021; A. Ferrara 2024), which lead to negative feedback, therefore reducing or even quenching the star formation (P. F. Hopkins et al. 2012). There might also exist an AGN in the compact E-core, which would be consistent with its high surface brightness and high dust temperature. In such a case, the E-core star formation history will be affected by additional negative feedback by AGN. Thus, the compact dusty starburst at the E-core may cease within several tens Myr.

The gas-phase metallicity for the entire system is estimated to be $\simeq 0.2 Z_\odot$ from the SED fitting, and these estimates are supported by the optical-to-FIR [O III] emission-line ratio. B14-65666 is on the average mass–metallicity relation at $z = 4$–9 (K. Nakajima et al. 2023; M. Curti et al. 2024), but given its high SFR, it would not be on the fundamental metallicity plane (B. H. Andrews & P. Martini 2013). Our analyses also show that galaxy E has lower metallicity than galaxy W, which is consistent with a scenario where a strong accretion of less-enriched gas dilutes the preexisting gas at the galaxy center (e.g., L. J. Kewley et al. 2006). At $Z_{\rm gas} \simeq 0.2 Z_\odot$, an ionization parameter estimated by Y. Sugahara et al. (2021) using the [O III] 88 μm and [C II] 158 μm lines is $\log U \simeq -2.0$, which is consistent with the SED fitting results. In other words, the high [O III]/[C II] ratio of B14-65666 can be naturally explained by the high ionization parameter (see T. Hashimoto et al. 2019; Y. Harikane et al. 2020). The [N II] 122 μm nondetection is also easily explained by the high ionization parameter where most of the nitrogen is in the doubly ionized phase (Y. Sugahara et al. 2021).

Finally, we mention some limitations of our observations. Although we have revealed many properties of the cores of the galaxies, fewer properties are constrained for the tails. This is mainly because it is difficult to solve the degeneracy in physics that can explain their red SED, dust nondetections, and detection of [O III] 88 μm emission, with different angular resolutions of the NIRCam and ALMA. We expected that the extended diffuse emission would originate from the tidal tails produced by the major merger, but we did not reject other possibilities like ionized gas outflows (e.g., S. Yuma et al. 2019) and offset old stellar populations (e.g., L. Colina et al. 2023). Approved MIRI and NIRSpec IFU spectroscopy and ALMA high-angular-resolution observations will give a hint to the properties of the tails. To reach statistical conclusions, a large sample of major mergers at high redshift is necessary. It is unclear whether B14-65666 is representative of major mergers at this redshift. Nevertheless, our results suggest that the major merger, which is an abundant population at high redshift (V. Rodriguez-Gomez et al. 2015; K. Duncan et al. 2019; M. Romano et al. 2021), makes significant contributions to galaxy mass assembly in the early Universe. B14-65666 is still an important target that provides us with detailed distributions of stellar, gaseous, and dust populations during major mergers.

6. Conclusions

In this paper, we present JWST NIRCam observations of the UV-bright ($M_{\rm UV} = -22.5$ mag) Lyman-break galaxy system B14-65666 at $z = 7.1520$, also known as the Big Three Dragons. The NIRCam filters are selected to sample the rest-frame UV wavelengths, the Balmer break clean of strong optical emission lines, and the rest-frame optical wavelengths ($\sim$5000 Å) including Hβ and [O III] emission lines. Additionally, rich ancillary ALMA data trace the [O III] 88 μm and [C II] 158 μm emission lines and underlying dust continua. The high angular resolution of these NIRCam and ALMA observations enables spatially resolved analyses at the rest-frame UV, optical, and FIR wavelengths of B14-65666, a bright major merger in the EoR.

B14-65666 consists of two galaxy components, E and W, and diffuse emission surrounding galaxy E. Galaxy E is red (UV spectral slope $\beta_{\rm UV} = -1.2$) and has a compact core (E-core) with an effective radius of $r_{\rm e} < 0''.016$ (85 pc) at the rest-frame 1400 Å. Galaxy W is blue ($\beta_{\rm UV} = -2.2$) and elongated to $\simeq 0''.3$ (1.5 kpc) with clumpy morphology in the rest-frame UV wavelengths. Surprisingly, in contrast to their colors, the blue galaxy W is brighter than the red galaxy E in the dust continua at 88 and 158 μm. The core of galaxy E (E-core) is surrounded by diffuse extended emission, which is only detected in the long NIRCam wavelength channels and is also bright in [O III] 88 μm. We assume that this extended emission is likely to be the tidal tails created by the gravitational interactions. Both galaxies E and W show the F444W flux excesses over the F356W fluxes ($0.84^{+0.09}_{-0.10}$ and $0.53^{+0.09}_{-0.10}$ mag, respectively), indicating the strong [O III] $\lambda\lambda$4960,5008 emission lines. The [O III] line map estimated from the F356W − F444W color traces strong [O III] emission at the E-core and W-core, with the rest-frame equivalent widths of $\mathrm{EW}_0 \simeq 2000$ and 750 Å, respectively. These results show that the major merger has disturbed the morphology of the galaxies and induced the nuclear dusty starbursts.

The SED fitting shows that B14-65666 has a total stellar mass of $\log M_*/M_\odot = 9.8 \pm 0.2$ and $\mathrm{SFR}_{\rm 10Myr}$ of $\simeq 230^{+70}_{-60} M_\odot$ yr^{-1}. These merger-induced starbursts would build young stellar masses comparable to or heavier than the underlying old stellar components. The stellar-mass ratio of galaxies E and W spans from 3:1 to 2:1, which confirms the fact that B14-65666 is a major merger in terms of the stellar-mass ratio. Galaxy E experiences young starbursts with $\mathrm{SFR}_{\rm 10Myr} = 180^{+50}_{-40} M_\odot$ yr^{-1} at ages of $<$53 Myr, supported by the high optical [O III] emission. The red color of galaxy E is explained by the strong dust attenuation of $A_{\rm V} = 1.2 \pm 0.1$ mag, opposite to galaxy W, which has a blue color and $A_{\rm V} = 0.3 \pm 0.1$ mag. Including ALMA data, the SED fitting explains the red color and faint dust continua of galaxy E by the scenario that galaxy E exhibits higher dust temperature than galaxy W.

As combinations of optical and FIR data, we investigate the IRX–$\beta_{\rm UV}$ diagram and the optical-to-FIR [O III] line ratios. The entire system is consistent with the $\beta_{\rm UV,0}$-modified Meurer relation, supporting the Calzetti attenuation law. Galaxies E and W, however, deviate from the relation; this deviation can be explained by different stellar and dust properties: variations of the dust attenuation law, patchy stellar-and-dust geometry, different dust temperatures, and possible effects of the tails. From the estimated [O III] $\lambda\lambda$4960,5008 map and the [O III] 88 μm moment-0 maps, we draw the optical-to-FIR [O III] line ratio map. This map illustrates a gradual spatial variation in the [O III] line ratio, implying spatial variation in the electron temperature and electron density. From the [O III] line ratios, the gas-phase metallicity of the entire galaxy is estimated to be $Z_{\rm gas} \sim 0.2$–$0.4 Z_\odot$ by photoionization models under the assumption of the electron density of $\sim$200 cm^{-3}. The E-core shows a higher [O III] line ratio than the W-core, indicating lower gas-phase metallicity in the E-core.

In summary, our results support a scenario where B14-65666 is a major merger that gravitationally disturbs the morphology and experiences nuclear dusty starbursts likely triggered by less-enriched gas inflows, after the first (or second) passage. Although galaxies E and W have similar UV magnitude, they exhibit different stellar, gaseous, and dust properties and morphology. The starbursts have indeed enhanced the star formation activity compared with main-sequence star-forming galaxies at the same redshift. B14-65666 is an important object that provides us with opportunities to investigate complex stellar buildup processes during major mergers, which are abundant at high redshifts, during the EoR.

Acknowledgments

We thank Rebecca Bowler for the helpful discussions on B14-65666. We wish to thank the anonymous referee for the valuable comments that improved our manuscript. This research is supported by NAOJ ALMA Scientific Research grant No. 2020-16B. This paper is a part of the outcome of research performed under a Waseda University Grant for Special Research Projects (Project number: 2024C-478). J.A.M., A.C.G., and L.C. acknowledge support by grant PIB2021-127718NB-100 from the Spanish Ministry of Science and Innovation/State Agency of Research MCIN/AEI/10.13039/501100011033 and by "ERDF A way of making Europe." T.H. was supported by the Leading Initiative for Excellent Young Researchers, MEXT, Japan (HJH02007) and by JSPS KAKENHI grant No. 22H01258. K. M., Y.N., and Y.T. acknowledge financial support from JSPS through KAKENHI grant Nos. 20K14516, 23KJ0728, and 22H04939, respectively. C.B.P. acknowledges support by grant CM21_CAB_M2_01 from the Program "Garantía Juvenil" from the "Comunidad de Madrid" 2021. MPS acknowledges support from grant RYC2021-033094-I funded by MCIN/AEI/10.13039/501100011033 and the European Union NextGenerationEU/

PRTR. The JWST data presented in this paper were obtained from the Mikulski Archive for Space Telescopes (MAST) at the Space Telescope Science Institute. The specific observations analyzed can be accessed via 10.17909/zps5-eq82. STScI is operated by the Association of Universities for Research in Astronomy, Inc., under NASA contract NAS5-26555. Support to MAST for these data is provided by the NASA Office of Space Science via grant NAG5-7584 and by other grants and contracts. This paper makes use of the following ALMA data: ADS/JAO.ALMA#2016.1.00954.S, ADS/JAO.ALMA#2017.1.00190.S, and ADS/JAO.ALMA#2019.1.01491.S. ALMA is a partnership of ESO (representing its member states), NSF (USA), and NINS (Japan), together with NRC (Canada), MOST and ASIAA (Taiwan), and KASI (Republic of Korea), in cooperation with the Republic of Chile. The Joint ALMA Observatory is operated by ESO, AUI/NRAO, and NAOJ. This work has made use of data from the European Space Agency (ESA) mission Gaia (https://www.cosmos.esa.int/gaia), processed by the Gaia Data Processing and Analysis Consortium (DPAC; https://www.cosmos.esa.int/web/gaia/dpac/consortium). Funding for the DPAC has been provided by national institutions, in particular, the institutions participating in the Gaia Multilateral Agreement. The Gaia data are retrieved from the JVO portal (http://jvo.nao.ac.jp/portal) operated by the NAOJ. This research has made use of NASA's Astrophysics Data System.

Software: NumPy (C. R. Harris et al. 2020), SciPy (P. Virtanen et al. 2020), IPython (F. Perez & B. E. Granger 2007), Matplotlib (J. D. Hunter 2007), Astropy (Astropy Collaboration et al. 2013, 2018, 2022).

Appendix
Supplements for the SED Fitting

Table A1 shows ranges of the free parameters in the SED fitting, explained in Section 3.2. `Bagpipes` receives these ranges as limits of the uniform prior distributions and performs the nested sampling to generate the posterior distribution of the parameters. Figure A1 shows a corner plot of an obtained posterior distribution in fitting to the total photometry including the ALMA data.

Table A2 shows results for fitting to the total photometry obtained with different parametric star formation histories: constant (fiducial), delayed τ, and exponential decreasing histories. The last row shows the fitting with the constant star formation history but without the old stellar component (i.e., without a parameter $M_{\rm old}$). All the star formation histories give comparable results because B14-65666 exhibits bursty star formation within a short timescale of $\sim$10 Myr.

Table A1
Parameter Ranges Used in the SED Fitting

Parameters	Ranges
$t_{\rm SF}$/Myr	[1.0, 300.0]
$\log M_*/M_\odot$	[1.0, 15.0]
$A_{\rm V}$/ mag	[0.0, 2.0]
$\log U$	[−4.0, −0.5]
$Z_*/Z_\odot$	[0.01, 2.00]
$\log M_{\rm old}/M_\odot$	[1.0, 15.0]
$\mathcal{U}_{\rm min}$	[0.1, 50.0]
γ	[0.001, 1.0]

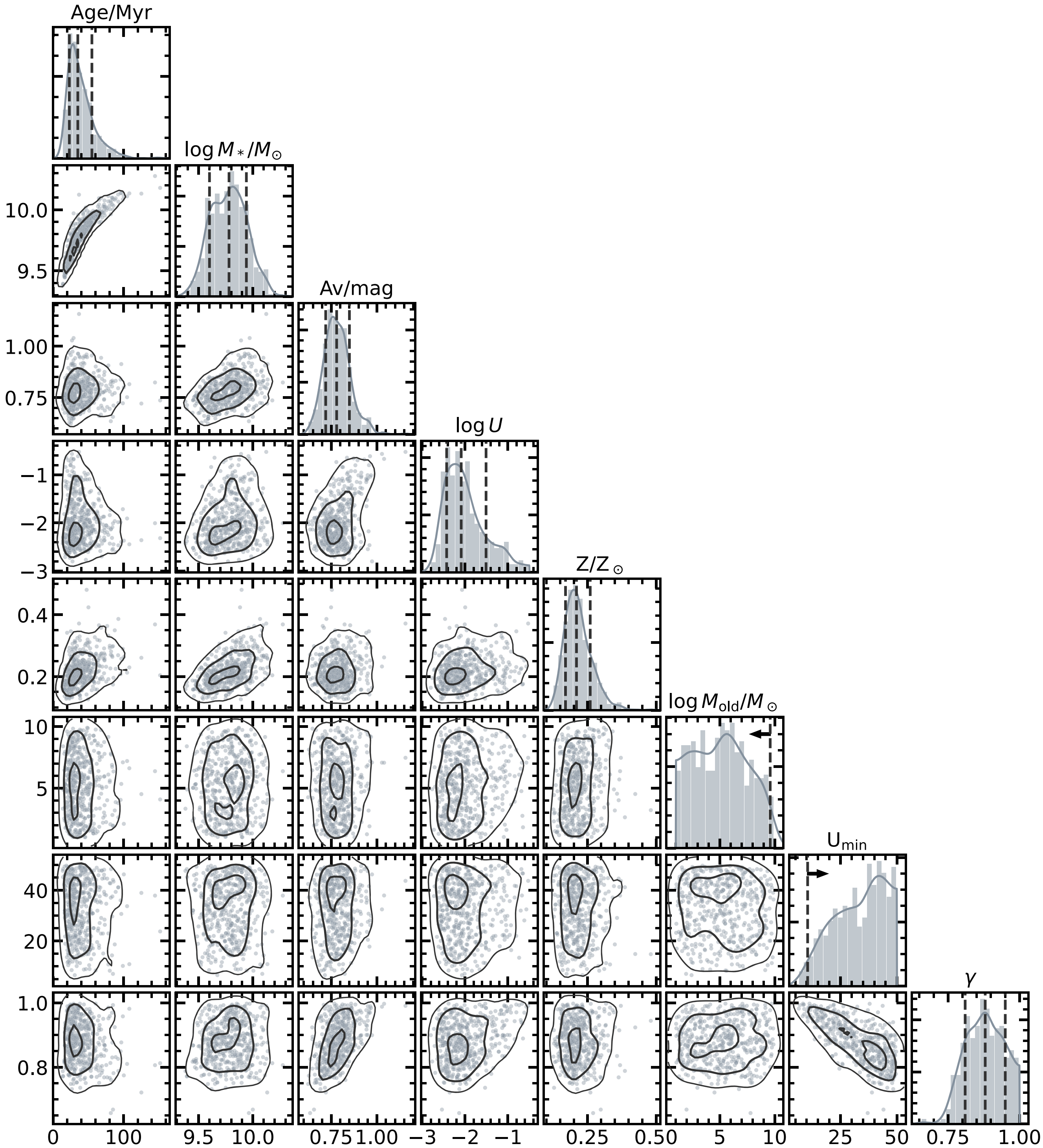

Figure A1 Corner plot for a result of the SED fitting to the total photometry including the ALMA data. The gray histograms show the posterior distribution of the fitting parameters and the gray curves show the kernel density estimations (KDE) of them. The vertical three black dashed lines indicate the 16, 50, and 84 percentiles of the posterior distribution of parameters, while the single dashed lines (with the arrows) indicate the 2σ lower/upper limits of parameters (i.e., 2/98 percentiles) for posterior distributions that hit to parameter limits and peak close to them. The scatter plots show correlations in the posterior distribution between the two parameters. The black contours show the 0.2σ, 1σ, and 2σ uncertainty regions computed with KDE.

Table A2
Results of the SED Fitting with Different Star Formation Histories and Setups

Components	τ (Myr)	$t_{\rm SF}$ (Myr)	$\log M_*$ ($\log M_\odot$)	$A_{\rm V}$ (mag(AB))	$\log U$	Z_* ($Z_\odot$)	$\log M_{\rm old}$ ($\log M_\odot$)
Constant	⋯	24^{+21}_{-9}	$9.75^{+0.18}_{-0.20}$	$0.87^{+0.13}_{-0.11}$	$-2.07^{+0.50}_{-0.35}$	$0.26^{+0.10}_{-0.07}$	<9.65
Delayed τ	185^{+73}_{-93}	29^{+29}_{-14}	$9.62^{+0.23}_{-0.19}$	$0.88^{+0.14}_{-0.12}$	$-2.08^{+0.57}_{-0.34}$	$0.28^{+0.10}_{-0.10}$	<9.61
Exponential	191^{+72}_{-93}	19^{+13}_{-8}	$9.69^{+0.17}_{-0.23}$	$0.89^{+0.13}_{-0.12}$	$-2.04^{+0.46}_{-0.38}$	$0.27^{+0.09}_{-0.09}$	<9.42
Constant (without old)	⋯	15^{+17}_{-9}	$9.60^{+0.25}_{-0.29}$	$0.90^{+0.17}_{-0.16}$	$-2.07^{+0.65}_{-0.36}$	$0.28^{+0.12}_{-0.11}$	⋯

Note. The results of the "Constant" star formation history (top) are the same as the "Total" with only NIRCam data in Table 4. The slight differences between them originate from the numerical uncertainties in the Monte Carlo computations.

ORCID iDs

Yuma Sugahara https://orcid.org/0000-0001-6958-7856
Javier Álvarez-Márquez https://orcid.org/0000-0002-7093-1877
Takuya Hashimoto https://orcid.org/0000-0002-0898-4038
Luis Colina https://orcid.org/0000-0002-9090-4227
Akio K. Inoue https://orcid.org/0000-0002-7779-8677
Luca Costantin https://orcid.org/0000-0001-6820-0015
Yoshinobu Fudamoto https://orcid.org/0000-0001-7440-8832
Ken Mawatari https://orcid.org/0000-0003-4985-0201
Yi W. Ren https://orcid.org/0000-0002-6510-5028
Santiago Arribas https://orcid.org/0000-0001-7997-1640
Tom J. L. C. Bakx https://orcid.org/0000-0002-5268-2221
Carmen Blanco-Prieto https://orcid.org/0009-0005-5448-5239
Daniel Ceverino https://orcid.org/0000-0002-8680-248X
Alejandro Crespo Gómez https://orcid.org/0000-0003-2119-277X
Masato Hagimoto https://orcid.org/0000-0001-8083-5814
Rui Marques-Chaves https://orcid.org/0000-0001-8442-1846
Hiroshi Matsuo https://orcid.org/0000-0003-3278-2484
Yurina Nakazato https://orcid.org/0000-0002-0984-7713
Miguel Pereira-Santaella https://orcid.org/0000-0002-4005-9619
Yoichi Tamura https://orcid.org/0000-0003-4807-8117
Naoki Yoshida https://orcid.org/0000-0001-7925-238X

References

Abdurro'uf, Coe, D., Jung, I., et al. 2023, ApJ, 945, 117
Abdurro'uf, Larson, R. L., Coe, D., et al. 2024, ApJ, 973, 47
Álvarez-Márquez, J., Burgarella, D., Buat, V., Ilbert, O., & Pérez-González, P. G. 2019, A&A, 630, A153
Álvarez-Márquez, J., Burgarella, D., Heinis, S., et al. 2016, A&A, 587, A122
Álvarez-Márquez, J., Crespo Gómez, A., Colina, L., et al. 2023, A&A, 671, A105
Álvarez-Márquez, J., Hashimoto, T., Arribas, S., et al. 2021, ALMA [OIII] 88 um Emitters. Signpost of Early Stellar Buildup and Reionization in the Universe, JWST Proposal. Cycle 1 #1840,
Anderson, J. 2016, Empirical Models for the WFC3/IR PSF, Instrument Science Report WFC3 2016-12,
Anderson, J., & King, I. R. 2000, PASP, 112, 1360
Andrews, B. H., & Martini, P. 2013, ApJ, 765, 140
Asada, Y., Sawicki, M., Abraham, R., et al. 2024, MNRAS, 527, 11372
Asplund, M., Amarsi, A. M., & Grevesse, N. 2021, A&A, 653, A141
Astropy Collaboration, Price-Whelan, A. M., Lim, P. L., et al. 2022, ApJ, 935, 167
Astropy Collaboration, Price-Whelan, A. M., Sipőcz, B. M., et al. 2018, AJ, 156, 123
Astropy Collaboration, Robitaille, T. P., Tollerud, E. J., et al. 2013, A&A, 558, A33
Bagley, M. B., Finkelstein, S. L., Koekemoer, A. M., et al. 2023, ApJL, 946, L12
Bakx, T. J. L. C., Sommovigo, L., Carniani, S., et al. 2021, MNRAS, 508, L58
Barnes, J. E., & Hernquist, L. 1996, ApJ, 471, 115
Barton, E. J., Geller, M. J., & Kenyon, S. J. 2000, ApJ, 530, 660
Bik, A., Álvarez-Márquez, J., Colina, L., et al. 2024, A&A, 686, A3
Boquien, M., Burgarella, D., Roehlly, Y., et al. 2019, A&A, 622, A103
Borne, K. D., Bushouse, H., Lucas, R. A., & Colina, L. 2000, ApJL, 529, L77
Boucaud, A., Bocchio, M., Abergel, A., et al. 2016, A&A, 596, A63
Bouwens, R. J., Oesch, P. A., Stefanon, M., et al. 2021, AJ, 162, 47
Bowler, R. A. A., Bourne, N., Dunlop, J. S., McLure, R. J., & McLeod, D. J. 2018, MNRAS, 481, 1631
Bowler, R. A. A., Cullen, F., McLure, R. J., Dunlop, J. S., & Avison, A. 2022, MNRAS, 510, 5088
Bowler, R. A. A., Dunlop, J. S., McLure, R. J., & McLeod, D. J. 2017, MNRAS, 466, 3612
Bowler, R. A. A., Dunlop, J. S., McLure, R. J., et al. 2012, MNRAS, 426, 2772
Bowler, R. A. A., Dunlop, J. S., McLure, R. J., et al. 2014, MNRAS, 440, 2810
Bowler, R. A. A., Inami, H., Sommovigo, L., et al. 2024, MNRAS, 527, 5808
Boyett, K., Bunker, A. J., Curtis-Lake, E., et al. 2024, MNRAS, 535, 1796
Bradley, L., Sipőcz, B. M., Robitaille, T., et al. 2023, astropy/photutils: v1.10.0, Zenodo, doi:10.5281/zenodo.596036
Burgarella, D., Bogdanoska, J., Nanni, A., et al. 2022, A&A, 664, A73
Bushouse, H., Eisenhamer, J., Dencheva, N., et al. 2023, JWST Calibration Pipeline v1.9.4, Zenodo, doi:10.5281/zenodo.7692609
Byrne, C. M., Stanway, E. R., Eldridge, J. J., McSwiney, L., & Townsend, O. T. 2022, MNRAS, 512, 5329
Calzetti, D., Armus, L., Bohlin, R. C., et al. 2000, ApJ, 533, 682
Calzetti, D., Kinney, A. L., & Storchi-Bergmann, T. 1994, ApJ, 429, 582
Carnall, A. C., McLure, R. J., Dunlop, J. S., & Davé, R. 2018, MNRAS, 480, 4379
CASA Team, Bean, B., Bhatnagar, S., et al. 2022, PASP, 134, 114501
Ceverino, D., Klessen, R. S., & Glover, S. C. O. 2018, MNRAS, 480, 4842
Ceverino, D., Mandelker, N., Snyder, G. F., et al. 2023, MNRAS, 522, 3912
Colina, L., Crespo Gómez, A., Álvarez-Márquez, J., et al. 2023, A&A, 673, L6
Costantin, L., Pérez-González, P. G., Vega-Ferrero, J., et al. 2023, ApJ, 946, 71
Crespo Gómez, A., Colina, L., Álvarez-Márquez, J., et al. 2024, A&A, 691, A325
Curti, M., Maiolino, R., Carniani, S., et al. 2024, A&A, 684, A75
Draine, B. T., Aniano, G., Krause, O., et al. 2014, ApJ, 780, 172
Draine, B. T., & Li, A. 2007, ApJ, 657, 810
Duan, Q., Conselice, C. J., Li, Q., et al. 2024, arXiv:2407.09472
Duncan, K., Conselice, C. J., Mundy, C., et al. 2019, ApJ, 876, 110
Eldridge, J. J., Stanway, E. R., Xiao, L., et al. 2017, PASA, 34, e058
Ellison, S. L., Patton, D. R., Simard, L., & McConnachie, A. W. 2008, AJ, 135, 1877
Fakhouri, O., & Ma, C.-P. 2008, MNRAS, 386, 577
Ferland, G. J., Chatzikos, M., Guzmán, F., et al. 2017, RMxAA, 53, 385
Ferland, G. J., Korista, K. T., Verner, D. A., et al. 1998, PASP, 110, 761
Ferrara, A. 2024, A&A, 684, A207
Finkelstein, S. L., Ryan, R. E., Jr., Papovich, C., et al. 2015, ApJ, 810, 71
Fudamoto, Y., Oesch, P. A., Faisst, A., et al. 2020, A&A, 643, A4
Fujimoto, S., Ouchi, M., Nakajima, K., et al. 2024, ApJ, 964, 146
Furusawa, H., Kashikawa, N., Kobayashi, M. A. R., et al. 2016, ApJ, 822, 46
Gaia Collaboration, Prusti, T., de Bruijne, J., H., J., et al. 2016, A&A, 595, A1
Gaia Collaboration, Vallenari, A., Brown, A. G. A., et al. 2023, A&A, 674, A1
García-Marín, M., Colina, L., Arribas, S., & Monreal-Ibero, A. 2009, A&A, 505, 1319
Gardner, J. P., Mather, J. C., Abbott, R., et al. 2023, PASP, 135, 068001
Giménez-Arteaga, C., Oesch, P. A., Brammer, G. B., et al. 2023, ApJ, 948, 126
Gordon, K. D., Clayton, G. C., Misselt, K. A., Landolt, A. U., & Wolff, M. J. 2003, ApJ, 594, 279
Groves, B. A., Dopita, M. A., & Sutherland, R. S. 2004, ApJS, 153, 9
Harikane, Y., Ouchi, M., Inoue, A. K., et al. 2020, ApJ, 896, 93

Harris, C. R., Jarrod Millman, K., van der Walt, S. J., et al. 2020, Natur, 585, 357
Hashimoto, T., Álvarez-Márquez, J., Fudamoto, Y., et al. 2023a, ApJL, 955, L2
Hashimoto, T., Inoue, A. K., Mawatari, K., et al. 2019, PASJ, 71, 71
Hashimoto, T., Inoue, A. K., Sugahara, Y., et al. 2023b, ApJ, 952, 48
Hodge, J. A., Riechers, D., Decarli, R., et al. 2015, ApJL, 798, L18
Hopkins, P. F., Hernquist, L., Cox, T. J., & Kereš, D. 2008, ApJS, 175, 356
Hopkins, P. F., Quataert, E., & Murray, N. 2012, MNRAS, 421, 3522
Hsiao, T. Y.-Y., Coe, D., Abdurro'uf, et al. 2023, ApJL, 949, L34
Hsiao, T. Y.-Y., Abdurro'uf, Coe, D., et al. 2024, ApJ, 973, 8
Hunter, J. D. 2007, CSE, 9, 90
Hygate, A. P. S., Hodge, J. A., da Cunha, E., et al. 2023, MNRAS, 524, 1775
Jones, G. C., Béthermin, M., Fudamoto, Y., et al. 2020a, MNRAS, 491, L18
Jones, T., Sanders, R., Roberts-Borsani, G., et al. 2020b, ApJ, 903, 150
Kewley, L. J., Geller, M. J., & Barton, E. J. 2006, AJ, 131, 2004
Kroupa, P. 2001, MNRAS, 322, 231
Li, J., Da Cunha, E., González-López, J., et al. 2024, ApJ, 976, 70
Liang, L., Feldmann, R., Kereš, D., et al. 2019, MNRAS, 489, 1397
Luridiana, V., Morisset, C., & Shaw, R. A. 2015, A&A, 573, A42
Man, A. W. S., Zirm, A. W., & Toft, S. 2016, ApJ, 830, 89
Mandelker, N., Dekel, A., Ceverino, D., et al. 2017, MNRAS, 464, 635
Marques-Chaves, R., Schaerer, D., Kuruvanthodi, A., et al. 2024, A&A, 681, A30
Marrone, D. P., Spilker, J. S., Hayward, C. C., et al. 2018, Natur, 553, 51
Matthee, J., Mackenzie, R., Simcoe, R. A., et al. 2023, ApJ, 950, 67
Merlin, E., Fontana, A., Ferguson, H. C., et al. 2015, A&A, 582, A15
Meurer, G. R., Heckman, T. M., & Calzetti, D. 1999, ApJ, 521, 64
Mihos, J. C., & Hernquist, L. 1994, ApJL, 425, L13
Mihos, J. C., & Hernquist, L. 1996, ApJ, 464, 641
Mushtaq, M., Ceverino, D., Klessen, R. S., Reissl, S., & Puttasiddappa, P. H. 2023, MNRAS, 525, 4976
Nakajima, K., Ouchi, M., Isobe, Y., et al. 2023, ApJS, 269, 33
Nakazato, Y., Ceverino, D., & Yoshida, N. 2024, ApJ, 975, 238
Nakazato, Y., Yoshida, N., & Ceverino, D. 2023, ApJ, 953, 140
Oke, J. B., & Gunn, J. E. 1983, ApJ, 266, 713
Ormerod, K., Conselice, C. J., Adams, N. J., et al. 2024, MNRAS, 527, 6110
Osterbrock, D. E., & Ferland, G. J. 2006, Astrophysics of Gaseous Nebulae and Active Galactic Nuclei (2nd. ed.; Sausalito, CA: University Science Books)
Oteo, I., Ivison, R. J., Dunne, L., et al. 2016, ApJ, 827, 34
Ouchi, M., Ellis, R., Ono, Y., et al. 2013, ApJ, 778, 102
Overzier, R. A., Heckman, T. M., Wang, J., et al. 2011, ApJL, 726, L7
Pereira-Santaella, M., Colina, L., García-Burillo, S., et al. 2021, A&A, 651, A42
Perez, F., & Granger, B. E. 2007, CSE, 9, 21
Pérez-González, P. G., Barro, G., Annunziatella, M., et al. 2023, ApJL, 946, L16
Planck Collaboration, Aghanim, N., Akrami, Y., et al. 2020, A&A, 641, A6
Popesso, P., Concas, A., Cresci, G., et al. 2023, MNRAS, 519, 1526
Popping, G., Puglisi, A., & Norman, C. A. 2017, MNRAS, 472, 2315
Prevot, M. L., Lequeux, J., Maurice, E., Prevot, L., & Rocca-Volmerange, B. 1984, A&A, 132, 389
Qu, Y., Helly, J. C., Bower, R. G., et al. 2017, MNRAS, 464, 1659
Reddy, N. A., Oesch, P. A., Bouwens, R. J., et al. 2018, ApJ, 853, 56
Ribeiro, B., Le Fèvre, O., Cassata, P., et al. 2017, A&A, 608, A16
Rieke, M. J., Kelly, D. M., Misselt, K., et al. 2023, PASP, 135, 028001
Rigby, J., Perrin, M., McElwain, M., et al. 2023, PASP, 135, 048001
Roberts-Borsani, G. W., Ellis, R. S., & Laporte, N. 2020, MNRAS, 497, 3440
Rodriguez-Gomez, V., Genel, S., Vogelsberger, M., et al. 2015, MNRAS, 449, 49
Romano, M., Cassata, P., Morselli, L., et al. 2021, A&A, 653, A111
Senchyna, P., Plat, A., Stark, D. P., & Rudie, G. C. 2024, ApJ, 966, 92
Shah, E. A., Kartaltepe, J. S., Magagnoli, C. T., et al. 2022, ApJ, 940, 4
Shapley, A. E., Sanders, R. L., Shao, P., et al. 2019, ApJL, 881, L35
Shibuya, T., Miura, N., Iwadate, K., et al. 2022, PASJ, 74, 73
Silva, A., Marchesini, D., Silverman, J. D., et al. 2018, ApJ, 868, 46
Snyder, G. F., Lotz, J. M., Rodriguez-Gomez, V., et al. 2017, MNRAS, 468, 207
Stanway, E. R., Eldridge, J. J., & Becker, G. D. 2016, MNRAS, 456, 485
Steidel, C. C., Rudie, G. C., Strom, A. L., et al. 2014, ApJ, 795, 165
Steidel, C. C., Strom, A. L., Pettini, M., et al. 2016, ApJ, 826, 159
Stiavelli, M., Morishita, T., Chiaberge, M., et al. 2023, ApJL, 957, L18
Sugahara, Y., Inoue, A. K., Fudamoto, Y., et al. 2022, ApJ, 935, 119
Sugahara, Y., Inoue, A. K., Hashimoto, T., et al. 2021, ApJ, 923, 5
Takeuchi, T. T., Yuan, F.-T., Ikeyama, A., Murata, K. L., & Inoue, A. K. 2012, ApJ, 755, 144
Tamura, Y., Bakx, T. J. L. C., Inoue, A. K., et al. 2023, ApJ, 952, 9
Treu, T., Calabrò, A., Castellano, M., et al. 2023, ApJL, 942, L28
Trussler, J. A. A., Adams, N. J., Conselice, C. J., et al. 2023, MNRAS, 523, 3423
Ventou, E., Contini, T., Bouché, N., et al. 2017, A&A, 608, A9
Virtanen, P., Gommers, R., Oliphant, T. E., et al. 2020, NatMe, 17, 261
Weaver, J. R., Kauffmann, O. B., Ilbert, O., et al. 2022, ApJS, 258, 11
Yang, S., & Lidz, A. 2020, MNRAS, 499, 3417
Yuma, S., Ouchi, M., Fujimoto, S., Kojima, T., & Sugahara, Y. 2019, ApJ, 882, 17